Hindawi
Structural Control and Health Monitoring
Volume 2024, Article ID 8896925, 27 pages
https://doi.org/10.1155/2024/8896925

Research Article

Feasibility Study of a Novel Modal Decomposition Method for Low-Frequency Structure with Nonproportionally Distributed Rate-Independent Linear Damping

Wei Liu,[1,2] **Yi-Qing Ni**,[1] **and Wai Kei Ao**[1]

[1]*Department of Civil and Environmental Engineering, The Hong Kong Polytechnic University, Hung Hom, Kowloon 999077, Hong Kong, China*
[2]*International Research Institute of Disaster Science, Tohoku University, Sendai 980-8572, Japan*

Correspondence should be addressed to Wei Liu; wei-r1.liu@polyu.edu.hk, Yi-Qing Ni; ceyqni@polyu.edu.hk, and Wai Kei Ao; waikei.ao@polyu.edu.hk

Received 19 May 2023; Revised 29 December 2023; Accepted 2 January 2024; Published 9 January 2024

Academic Editor: Yoshiki Ikeda

Compared with conventional linear viscous damping (LVD), rate-independent linear damping (RILD) mitigates floor response acceleration in low-frequency structures more effectively without compromising the control performance of displacement responses during long-period or low-frequency earthquakes. Although theoretical and experimental attempts have been made to overcome the noncausality of RILD devices and realize RILD using passive or semiactive devices, only a few studies have highlighted the impulse-response precursor and modal analysis method of multistory structures incorporated into RILD devices. This study investigated the impulse-response precursor of a noncausal RILD system and proposed a novel modal decomposition method for the structures equipped with nonproportionally distributed RILD devices. Additionally, real-time hybrid simulation was conducted to validate the effectiveness of the proposed modal analysis method and the feasibility of realizing ideal RILD using mechanical devices. This study is the first to demonstrate the differences between RILD and LVD devices in terms of controlling the modal responses of low-frequency structures and how RILD can lower the floor response acceleration more effectively compared to LVD.

1. Introduction

The earthquake that occurred in the Tohoku region of East Japan in 2011 resulted in many high-rise and base-isolated buildings experiencing long-duration and large-amplitude shaking, causing destructive damage to their surroundings and internal equipment. Therefore, those excessive displacements should be investigated and avoided. Low-frequency buildings can be made more seismically resilient through rate-independent linear damping (RILD) [1]. However, RILD has not been implemented in actual projects because of its noncausality, as explained by Crandall [2, 3] and Inaudi and Kelly [4].

RILD, also referred to as structural damping, complex damping, complex stiffness, and hysteretic damping, has been studied since the mid-20th century. According to Myklestad [5], one of the biggest advantages of complex damping is that it enables numerical calculations of forced vibrations in engine crankshafts, airplane wings, and similar structures. Bishop [6] argued that free vibrations cannot be treated satisfactorily unless hysteretic damping can cover nonharmonic motions. The first causal model resembling RILD was proposed by Biot [7]. However, Caughey [8] demonstrated that Biot's model and RILD are not identical at low frequencies. Makris and Constantinou [9] employed the fractional-derivative Maxwell model of viscous dampers for seismic isolation of buildings. Muravskii [10] investigated three nonlinear models with frequency-independent characteristics. Nakamura [11] developed a causal model for hysteretic damping. Spanos and

Tsavachidis [12] performed analyses of a nonlinear system with a Biot viscoelastic element. Makris [13] used an adjustable term to satisfy the causality requirements. In addition, studies have proposed mathematical models to approximate the behavior of RILD [14, 15]. Muravskii [16] reported that Biot's model and three hereditary models can ensure the practical constancy for damping properties but are limited to the storage stiffness as the frequency grows. Huang et al. [17] proposed a frequency-insensitive damping model that exhibits constant energy dissipation over an interest-frequency range; however, this model still lacks experimental verification.

An RILD model was developed by Genta and Amanti [18] by placing several Maxwell elements in parallel. Reggio and De Angelis [19] employed the Maxwell–Wiechert kernel function to propose a viscoelastic model to realize RILD. Deastra et al. [20] introduced two inerter-based dampers to capture the behavior of RILD. Sarlis et al. [21, 22] developed physical devices to achieve negative stiffness, which is a significant component for some causal RILD models. Nagarajaiah et al. [23] investigated the multimode response mitigation effects of dampers with negative stiffness and inerter systems. Luo et al. [24] used a Maxwell negative-stiffness damper to causally realize RILD. Keivan et al. [25, 26] approximated the RILD storage stiffness using a digital filter. Keivan et al. [27] then incorporated the proposed filter into the interstory isolated structure without considering the impact of vertical vibrations. Liu and Ikago [28] proposed a modified RILD model that could achieve better performance in terms of mimicking the loss stiffness. Liu et al. [29] developed three models to realize an ideal RILD and improve the performance of a higher-order filter [28]. Liu and Ikago [30–33] were the first to conduct real-time hybrid testing using mechanical devices to passively realize a noncausal RILD device. Recently, Liu and Liu [34] conducted the first experiment to realize a modified RILD model [29] using a small-scale MR damper. Liu et al. [35] further developed two causal RILD models and proposed both the optimal and direct design methods for these two devices.

Inaudi and Makris [36] investigated a time-domain method for numerical analysis of the RILD system using the characteristics of the Hilbert transform. Tsai and Lee [37] developed a method for obtaining the transient response of oscillators using RILD. Studies have also used the integral contour method to study the impulse-response precursor of a building containing a hysteretic damper [38, 39].

The existing literature shows several existing modal analysis methods for classically damped systems [40, 41]. Chopra [42] presented the physical interpretation of the modal analysis of linear systems. Ewins [43] showed the modal testing of structures based on modal analysis. William et al. [44] systematically presented the matrix structural analysis method. However, the above literature mainly focused on the classically damped systems. Veletsos and Ventura [45] proposed a method for the modal decomposition of nonclassically damped systems, which was then adopted in textbooks [46]. Igusa and Kiureghian [47] derived solutions for the mode shapes and frequencies. Yang et al. [48] proposed a response spectrum method. Several other techniques have been widely used to assess the maximum responses of damped structures [49]. Gupta et al. [50] assessed the performance of nonclassically damped systems for different frequency ranges. Oliveto et al. [51] proposed a complex mode superposition method for analyzing the dynamic behavior of a beam supported by and attached to two rotational dampers. Lorenzo et al. [52] proposed a method for analyzing the vibration response of beams with Kelvin–Voigt viscoelastic translational supports and rotational joints under moving loads. Hirzinger et al. [53] developed a semianalytical method to determine the dynamic response of an Euler–Bernoulli beam under general boundary conditions. Chen et al. [54] suggested a generalized mode superposition method that could be applied to damping at undercritical, critical, and overcritical levels. Qiao and Rahmatalla [55] devised a novel method to determine the viscoelastic boundary conditions and dynamic responses of Euler–Bernoulli beams under changing loads. Chen et al. [56] proposed a complex-model truncation approach. However, the aforementioned modal analysis method cannot be applied to the noncausal RILD systems.

It has been reported that RILD can more effectively suppress the acceleration responses of low-frequency structures without or only slightly compromising the mitigation of displacement responses. However, limited research has been found so far to investigate the differences in seismic responses between the RILD and linear viscous damping (LVD) systems based on modal analysis. Furthermore, no study has focused on the performance of the nonproportionally distributed RILD systems. This study obtained the impulse-response precursor of a noncausal RILD system and first revealed differences in the modal responses of structures containing RILD and LVD. Furthermore, a novel modal decomposition method is proposed to obtain the modal responses of structures equipped with nonproportionally distributed RILD devices, thereby providing a novel approach for time-domain analysis of the RILD system. This study first creates a link between the modal analysis of the LVD and RILD systems. Upon employing the proposed method, the differences in dynamic responses between the LVD and RILD systems can be clearly observed, thus demonstrating the advantages of RILD for the seismic protection of low-frequency structures. To validate the observation of numerical analysis, real-time hybrid simulations were also conducted by employing physical devices, including a coil spring and an oil damper.

The remainder of this paper is structured as follows: Section 2 derives the expression of the impulse-response precursor and presents a modal decomposition technique for a nonproportionally distributed multi-degree-of-freedom (MDOF) RILD system. Section 3 describes the application of the proposed method for conducting numerical analyses to investigate the differences between the control effects of the two different damping devices. Section 4 describes the fabrication of a coil spring and an oil damper for physically realizing noncausal RILD and experimentally verifying the proposed modal decomposition method. Finally, Section 5 presents the conclusions of this study and discusses the potential challenges and future scopes.

2. Modal Decomposition Method of the RILD System

Owing to the well-known noncausality of RILD, the conventional modal superposition technique discussed in [45, 46] for nonclassically damped systems cannot be used on a structure containing RILD elements. Causality requires the response to follow the application of excitation. As shown in Figure 1, the RILD system responded before the excitation was applied, which violated the causality requirement. This study proposes a modal decomposition method to approximate the responses of a noncausal RILD system.

When an ideal RILD device with loss stiffness ηk is subjected to harmonic load, its damping force can be calculated as follows [57]:

$$F_{\mathrm{RILD}} = i\eta k sgn[\mathrm{Re}(\omega)]X(i\omega), \tag{1}$$

where F_{RILD}, i, $\mathrm{sgn}(\cdot)$, $\mathrm{Re}(\cdot)$, and $X(i\omega)$ denote the damping force amplitude, imaginary unit, signum function, the real part of the complex number, and displacement response amplitude, respectively.

2.1. Impulse-Response Precursor. As mentioned above, when the structure is incorporated with noncausal RILD and subjected to impulse excitation, the response advances the application of impulsive excitation. Therefore, the RILD system has nonzero displacements in the negative time region ($t < 0$), which is referred to as the impulse-response precursor in this study. To date, no studies have been conducted on the impulse-response precursors of multistory RILD systems. Thus, the expression of the impulse-response precursor must be deduced before investigating the modal decomposition method of the RILD system.

The base-isolated shear MDOF system is assumed to be incorporated with nonproportional RILD, and the loss factors of the RILD are η_j ($j = 1, 2, \cdots, n. n \geq 2$) for the j – th floor. η_1 and η_n are the base-isolation layer and roof floor loss factor, respectively. The equation of motion that controls the nonproportional RILD system is given as follows:

$$\mathbf{M}\ddot{\mathbf{X}} + \mathbf{C}\dot{\mathbf{X}} + \mathbf{K}\mathbf{X} = -\mathbf{M}\mathbf{r}\ddot{x}_g, \tag{2}$$

where $\mathbf{M}$, $\mathbf{C}$, $\mathbf{K}$, $\ddot{\mathbf{X}}$, $\dot{\mathbf{X}}$, and $\mathbf{X}$ are the matrices for mass, inherent damping, complex stiffness, floor response acceleration, relative velocity, and relative displacement, respectively. $\mathbf{r}$ and $\ddot{x}_g$ represent the influence vector and ground acceleration, respectively.

Equation (2) can be converted as follows:

$$\left(-\omega^2\mathbf{M} + i\omega\mathbf{C} + \mathbf{K}\right)\mathbf{X}(i\omega) = -\mathbf{M}\mathbf{r}\ddot{x}_g(i\omega). \tag{3}$$

Then,

$$\frac{\mathbf{X}(i\omega)}{-\ddot{x}_g(i\omega)} = \frac{\mathbf{M}\mathbf{r}}{-\omega^2\mathbf{M} + i\omega\mathbf{C} + \mathbf{K}} = \frac{\mathbf{I}\mathbf{r}}{-\omega^2\mathbf{I} + i\omega\mathbf{M}^{-1}\mathbf{C} + \mathbf{M}^{-1}\mathbf{K}}, \tag{4}$$

where $\mathbf{I}$ is the identity matrix. The symbols in equation (4) can be expressed as follows:

$$\mathbf{M} = \begin{bmatrix} m_1 & 0 & \cdots & 0 & 0 \\ 0 & m_2 & \cdots & 0 & 0 \\ \vdots & \vdots & \ddots & \vdots & \vdots \\ 0 & 0 & \cdots & m_{n-1} & 0 \\ 0 & 0 & \cdots & 0 & m_n \end{bmatrix}, \mathbf{C} = \begin{bmatrix} c_1 + c_2 & -c_2 & \cdots & 0 & 0 \\ -c_2 & c_2 + c_3 & \cdots & 0 & 0 \\ \vdots & \vdots & \ddots & \vdots & \vdots \\ 0 & 0 & \cdots & c_{n-1} + c_n & -c_n \\ 0 & 0 & \cdots & -c_n & c_n \end{bmatrix},$$

$$\mathbf{K} = \mathbf{K_0} + i\mathrm{sgn}(\omega)\mathbf{K}',$$

$$\mathbf{K_0} = \begin{bmatrix} k_1 + k_2 & -k_2 & \cdots & 0 & 0 \\ -k_2 & k_2 + k_3 & \cdots & 0 & 0 \\ \vdots & \vdots & \ddots & \vdots & \vdots \\ 0 & 0 & \cdots & k_{n-1} + k_n & -k_n \\ 0 & 0 & \cdots & -k_n & k_n \end{bmatrix}, \tag{5}$$

$$\mathbf{K}' = \begin{bmatrix} \eta_1 k_1 + \eta_2 k_2 & -\eta_2 k_2 & \cdots & 0 & 0 \\ -\eta_2 k_2 & \eta_2 k_2 + \eta_3 k_3 & \cdots & 0 & 0 \\ \vdots & \vdots & \ddots & \vdots & \vdots \\ 0 & 0 & \cdots & \eta_{n-1} k_{n-1} + \eta_n k_n & -\eta_n k_n \\ 0 & 0 & \cdots & -\eta_n k_n & \eta_n k_n \end{bmatrix},$$

$$\mathbf{r} = \begin{bmatrix} 1 & 1 & \cdots & 1 & 1 \end{bmatrix}^T.$$

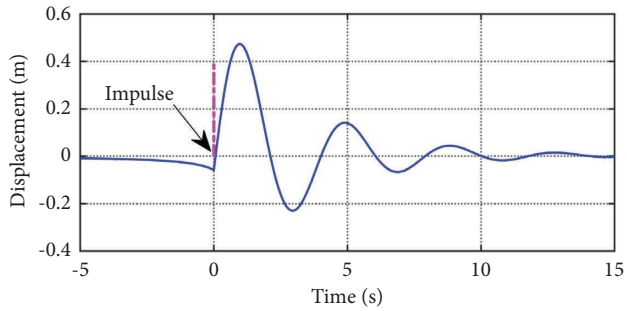

Figure 1: Impulse response of the rate-independent linear damping (RILD) system with a single degree of freedom (natural period of 4 s).

Here, $\eta_1, \eta_2, \ldots, \eta_n$ are the loss factors (double the damping ratio) of the base-isolation layer, first floor, . . ., and roof-floor, respectively.

In principle, the RILD system's impulse-response function is stated as follows:

$$h(t) = \frac{1}{2\pi}\int_{-\infty}^{+\infty} \frac{\mathbf{X}(i\omega)}{-\ddot{x}_g(i\omega)} e^{i\omega t} d\omega = \frac{1}{2\pi}\int_{-\infty}^{+\infty} \frac{\mathbf{I}\mathbf{r} e^{i\omega t}}{-\omega^2\mathbf{I} + i\omega\mathbf{M}^{-1}\mathbf{C} + \mathbf{M}^{-1}\mathbf{K}} d\omega. \tag{6}$$

Therefore,

$$\begin{aligned} h(t) &= \frac{1}{2\pi}\int_{-\infty}^{+\infty} \frac{\mathbf{I}\mathbf{r} e^{i\omega t}}{-\omega^2\mathbf{I} + i\omega\mathbf{M}^{-1}\mathbf{C} + \mathbf{M}^{-1}\mathbf{K}} d\omega \\ &= \frac{1}{2\pi}\int_{-\infty}^{+\infty} \frac{\mathbf{I}\mathbf{r} e^{i\omega t}}{-\omega^2\mathbf{I} + \mathbf{M}^{-1}\mathbf{K_0} + i\left[\omega\mathbf{M}^{-1}\mathbf{C} + \operatorname{sgn}(\omega)\mathbf{M}^{-1}\mathbf{K}'\right]} d\omega \\ &= \frac{1}{2\pi}\int_{-\infty}^{+\infty} \frac{\left(-\omega^2\mathbf{I} + \mathbf{M}^{-1}\mathbf{K_0} - i\left[\omega\mathbf{M}^{-1}\mathbf{C} + \operatorname{sgn}(\omega)\mathbf{M}^{-1}\mathbf{K}'\right]\right)\mathbf{I}\mathbf{r} e^{i\omega t}}{\left(-\omega^2\mathbf{I} + \mathbf{M}^{-1}\mathbf{K_0}\right)^2 + \left[\omega\mathbf{M}^{-1}\mathbf{C} + \operatorname{sgn}(\omega)\mathbf{M}^{-1}\mathbf{K}'\right]^2} d\omega \\ &= \frac{1}{2\pi}\int_{-\infty}^{+\infty} \frac{\left(-\omega^2\mathbf{I} + \mathbf{M}^{-1}\mathbf{K_0} - i\left[\omega\mathbf{M}^{-1}\mathbf{C} + \operatorname{sgn}(\omega)\mathbf{M}^{-1}\mathbf{K}'\right]\right)\mathbf{I}\mathbf{r} e^{i\omega t}}{\left(-\omega^2\mathbf{I} + \mathbf{M}^{-1}\mathbf{K_0}\right)^2 + \left(\omega\mathbf{M}^{-1}\mathbf{C}\right)^2 + \left(\mathbf{M}^{-1}\mathbf{K}'\right)^2 + 2|\omega|\mathbf{M}^{-1}\mathbf{C}\mathbf{M}^{-1}\mathbf{K}'} d\omega. \end{aligned} \tag{7}$$

Considering the numerator part of the integral function of equation (7) yields

$$\begin{aligned} \text{Numerator} &= \left(-\omega^2\mathbf{I} + \mathbf{M}^{-1}\mathbf{K_0} - i\left[\omega\mathbf{M}^{-1}\mathbf{C} + \operatorname{sgn}(\omega)\mathbf{M}^{-1}\mathbf{K}'\right]\right)\mathbf{I}\mathbf{r} e^{i\omega t} \\ &= \left(-\omega^2\mathbf{I} + \mathbf{M}^{-1}\mathbf{K_0} - i\left[\omega\mathbf{M}^{-1}\mathbf{C} + \operatorname{sgn}(\omega)\mathbf{M}^{-1}\mathbf{K}'\right]\right)\mathbf{I}\mathbf{r}(\cos\omega t + i\sin\omega t) \\ &= e_1(t) + e_2(t), \end{aligned} \tag{8}$$

where

$$e_1(t) = \left[\left(-\omega^2\mathbf{I} + \mathbf{M}^{-1}\mathbf{K_0}\right)\cos\omega t + \omega\mathbf{M}^{-1}\mathbf{C}\sin\omega t + \operatorname{sgn}(\omega)\sin\omega t\mathbf{M}^{-1}\mathbf{K}'\right]\mathbf{Ir},$$
$$e_2(t) = i\left[\left(-\omega^2\mathbf{I} + \mathbf{M}^{-1}\mathbf{K_0}\right)\sin\omega t - \omega\mathbf{M}^{-1}\mathbf{C}\cos\omega t - \operatorname{sgn}(\omega)\cos\omega t\mathbf{M}^{-1}\mathbf{K}'\right]\mathbf{Ir}. \tag{9}$$

It is obvious that $e_1(t)$ and $e_2(t)$ are even and odd functions, respectively. Therefore,

$$\begin{aligned}
h(t) &= \frac{1}{2\pi}\int_{-\infty}^{+\infty}\frac{\left(-\omega^2\mathbf{I} + \mathbf{M}^{-1}\mathbf{K_0} - i\left[\omega\mathbf{M}^{-1}\mathbf{C} + \operatorname{sgn}(\omega)\mathbf{M}^{-1}\mathbf{K}'\right]\right)\mathbf{Ir}e^{i\omega t}}{\left(-\omega^2\mathbf{I} + \mathbf{M}^{-1}\mathbf{K_0}\right)^2 + \left(\omega\mathbf{M}^{-1}\mathbf{C}\right)^2 + \left(\mathbf{M}^{-1}\mathbf{K}'\right)^2 + 2|\omega|\mathbf{M}^{-1}\mathbf{C}\mathbf{M}^{-1}\mathbf{K}'}d\omega \\
&= \frac{1}{2\pi}\int_{-\infty}^{+\infty}\frac{e_1(t)}{\left(-\omega^2\mathbf{I} + \mathbf{M}^{-1}\mathbf{K_0}\right)^2 + \left(\omega\mathbf{M}^{-1}\mathbf{C}\right)^2 + \left(\mathbf{M}^{-1}\mathbf{K}'\right)^2 + 2|\omega|\mathbf{M}^{-1}\mathbf{C}\mathbf{M}^{-1}\mathbf{K}'}d\omega \\
&\quad + \frac{1}{2\pi}\int_{-\infty}^{+\infty}\frac{e_2(t)}{\left(-\omega^2\mathbf{I} + \mathbf{M}^{-1}\mathbf{K_0}\right)^2 + \left(\omega\mathbf{M}^{-1}\mathbf{C}\right)^2 + \left(\mathbf{M}^{-1}\mathbf{K}'\right)^2 + 2|\omega|\mathbf{M}^{-1}\mathbf{C}\mathbf{M}^{-1}\mathbf{K}'}d\omega \\
&= \frac{1}{2\pi}\int_{-\infty}^{+\infty}\frac{e_1(t)}{\left(-\omega^2\mathbf{I} + \mathbf{M}^{-1}\mathbf{K_0}\right)^2 + \left(\omega\mathbf{M}^{-1}\mathbf{C}\right)^2 + \left(\mathbf{M}^{-1}\mathbf{K}'\right)^2 + 2|\omega|\mathbf{M}^{-1}\mathbf{C}\mathbf{M}^{-1}\mathbf{K}'}d\omega + 0 \\
&= \frac{1}{\pi}\int_{0}^{+\infty}\frac{\left[\left(-\omega^2\mathbf{I} + \mathbf{M}^{-1}\mathbf{K_0}\right)\cos\omega t + \omega\mathbf{M}^{-1}\mathbf{C}\sin\omega t + \operatorname{sgn}(\omega)\sin\omega t\mathbf{M}^{-1}\mathbf{K}'\right]\mathbf{Ir}}{\left(-\omega^2\mathbf{I} + \mathbf{M}^{-1}\mathbf{K_0}\right)^2 + \left(\omega\mathbf{M}^{-1}\mathbf{C}\right)^2 + \left(\mathbf{M}^{-1}\mathbf{K}'\right)^2 + 2|\omega|\mathbf{M}^{-1}\mathbf{C}\mathbf{M}^{-1}\mathbf{K}'}d\omega \\
&= \frac{1}{\pi}\int_{0}^{+\infty}\frac{\left[\left(-\omega^2\mathbf{I} + \mathbf{M}^{-1}\mathbf{K_0}\right)\cos\omega t + \omega\mathbf{M}^{-1}\mathbf{C}\sin\omega t + \sin\omega t\mathbf{M}^{-1}\mathbf{K}'\right]\mathbf{Ir}}{\left(-\omega^2\mathbf{I} + \mathbf{M}^{-1}\mathbf{K_0}\right)^2 + \left(\omega\mathbf{M}^{-1}\mathbf{C}\right)^2 + \left(\mathbf{M}^{-1}\mathbf{K}'\right)^2 + 2|\omega|\mathbf{M}^{-1}\mathbf{C}\mathbf{M}^{-1}\mathbf{K}'}d\omega.
\end{aligned} \tag{10}$$

As shown in equation (10), the derived impulse-response expression $h(t)$ can be employed to obtain the impulse-response precursors in both structures with or without inherent viscous damping. However, for comparison and simplicity, a simpler expression can be obtained as follows while neglecting inherent viscous damping (i.e., $\mathbf{C} = \mathbf{0}$):

$$h(t) = \frac{1}{\pi}\int_{0}^{+\infty}\frac{\left[\left(-\omega^2\mathbf{I} + \mathbf{M}^{-1}\mathbf{K_0}\right)\cos\omega t + \sin\omega t\mathbf{M}^{-1}\mathbf{K}'\right]\mathbf{Ir}}{\left(-\omega^2\mathbf{I} + \mathbf{M}^{-1}\mathbf{K_0}\right)^2 + \left(\mathbf{M}^{-1}\mathbf{K}'\right)^2}d\omega. \tag{11}$$

When the system only has one degree of freedom, $h(t)$ is reduced to

$$h(t) = \frac{1}{\pi}\int_{0}^{+\infty}\frac{\left(-\omega^2 + \omega_1^2\right)\cos\omega t + \eta_1\omega_1^2\sin\omega t}{\left(-\omega^2 + \omega_1^2\right)^2 + \left(\eta_1\omega_1^2\right)^2}d\omega, \tag{12}$$

where ω_1 is the first natural frequency.

Equation (12) is identical to that obtained by Inaudi and Kelly [4] who employed the inverse Fourier transform to calculate the response history of the RILD system with only one degree of freedom and without inherent damping. Finally, equations (10) or (11) can be used to retrieve the

impulse-response precursors of the RILD system that have more than one degree of freedom with or without considering inherent damping, respectively.

A single-story base-isolated shear structure was used as the building model, and three types of damping systems were considered, as shown in Figure 2. The LVD and RILD systems were nonproportionally damped, and the damping ratios of the supplemental damping devices were assumed to be identical.

The modal analysis method presented in [45, 46] can be applied directly to undamped LVD systems. In the following phase, a modal decomposition method is developed for an RILD system that is not proportionally damped.

2.2. Free Vibration Response. The homogeneous form of equation (2) yields [45, 46]

$$\mathbf{X}(t) = \boldsymbol{\psi} e^{\lambda t}. \tag{13}$$

Equation (14) can be obtained by converting equation (13) into the homogeneous form of equation (2) as follows:

$$\left(\lambda^2 \mathbf{M} + \lambda \mathbf{C} + \mathbf{K}\right)\boldsymbol{\psi} = \mathbf{0}. \tag{14}$$

Reducing the N-dimensional second-order differential equation (equation (2)) to the $2N$-dimensional first-order differential equations, we obtain as follows [58]:

$$\begin{aligned} \mathbf{M}\dot{\mathbf{X}} - \mathbf{M}\dot{\mathbf{X}} &= \mathbf{0} \\ \mathbf{M}\ddot{\mathbf{X}} + \mathbf{C}\dot{\mathbf{X}} + \mathbf{K}\mathbf{X} &= -\mathbf{M}\mathbf{r}\ddot{x}_g \end{aligned}. \tag{15}$$

Therefore,

$$\mathbf{L}\dot{\mathbf{Z}} + \mathbf{S}\mathbf{Z} = \mathbf{p}(\mathbf{t}), \tag{16}$$

where

$$\mathbf{L} = \begin{bmatrix} \mathbf{0} & \mathbf{M} \\ \mathbf{M} & \mathbf{C} \end{bmatrix}, \mathbf{S} = \begin{bmatrix} -\mathbf{M} & \mathbf{0} \\ \mathbf{0} & \mathbf{K} \end{bmatrix}, \mathbf{Z} = \begin{bmatrix} \dot{\mathbf{X}} \\ \mathbf{X} \end{bmatrix}, \mathbf{p}(\mathbf{t}) = \begin{bmatrix} \mathbf{0} \\ -\mathbf{M}\mathbf{r}\ddot{x}_g \end{bmatrix}. \tag{17}$$

Regarding the RILD system shown in Figure 2(c), we obtain

$$\mathbf{M} = \begin{bmatrix} m & 0 \\ 0 & m \end{bmatrix}, \tag{18}$$

$$\mathbf{K}^{+} = \begin{bmatrix} k_1 + k_2 + i(\eta_1 k_1 + \eta_2 k_2) & -(1 + i\eta_2)k_2 \\ -(1 + i\eta_2)k_2 & (1 + i\eta_2)k_2 \end{bmatrix}, \omega > 0, \tag{19}$$

$$\mathbf{K}^{-} = \begin{bmatrix} k_1 + k_2 - i(\eta_1 k_1 + \eta_2 k_2) & -(1 - i\eta_2)k_2 \\ -(1 - i\eta_2)k_2 & (1 - i\eta_2)k_2 \end{bmatrix}, \omega < 0. \tag{20}$$

As shown in equations (19) and (20), the stiffness matrix was divided into two cases owing to the presence of the signum function ($\mathrm{sgn}(\omega) > 0$, for $\omega > 0$ and $\mathrm{sgn}(\omega) < 0$, for $\omega < 0$).

Substituting equations (18) and (20) into the homogeneous forms of equation (16) yields

$$\mathbf{L}\dot{\mathbf{Z}} + \mathbf{S}^{\pm}\mathbf{Z} = \mathbf{0}, \tag{21}$$

$$\mathbf{S}^{\pm} = \begin{bmatrix} -\mathbf{M} & \mathbf{O} \\ \mathbf{O} & \mathbf{K}^{\pm} \end{bmatrix}, \tag{22}$$

where superscripts "+" and "−" denote positive ($\omega > 0$) and negative ($\omega < 0$) excitation frequencies, respectively.

The eigenvalues and eigenvectors are given as follows:

$$\boldsymbol{\lambda}^{\pm} = \begin{bmatrix} \lambda_1^{\pm} & \lambda_2^{\pm} & \widehat{\lambda}_1^{\pm} & \widehat{\lambda}_2^{\pm} \end{bmatrix}^T, \tag{23}$$

$$\boldsymbol{\psi}^{\pm} = \begin{bmatrix} \boldsymbol{\psi}_1^{\pm} & \boldsymbol{\psi}_2^{\pm} & \widehat{\boldsymbol{\psi}}_1^{\pm} & \widehat{\boldsymbol{\psi}}_2^{\pm} \end{bmatrix}, \tag{24}$$

where the hat symbol denotes the modes related to the unstable poles (where the real parts of the related eigenvalues are positive). It is worth mentioning that equations (23) and (24) are only applicable to the 2DOF system. The related eigenvalues and eigenvectors for the n-DOF structure can be obtained in a similar manner.

Therefore, four ($2N$) sets of eigenvalues and eigenvectors for the stable and unstable poles exist. In the following section, we prove that the conjugate eigenvalues and eigenvectors for $\omega > 0$ can be determined from the case of $\omega < 0$.

Regarding the nth pair of eigenvalue and eigenvector, we obtain

$$\left(\lambda_n^{+}\mathbf{L} + \mathbf{S}^{+}\right)\boldsymbol{\upsilon}_n^{+} = \mathbf{0}, \boldsymbol{\upsilon}_n^{+} = \begin{bmatrix} \lambda_n^{+}\boldsymbol{\psi}_n^{+} \\ \boldsymbol{\psi}_n^{+} \end{bmatrix}^T. \tag{25}$$

Considering $\overline{\mathbf{S}}^{+} = \mathbf{S}^{-}$ (which can be proved by employing equations (18), (19), and (22)) and the complex conjugate on both sides of the first part of equation (25), we obtain

$$\left(\overline{\lambda}_n^{+}\mathbf{L} + \mathbf{S}^{-}\right)\overline{\boldsymbol{\upsilon}}_n^{+} = \mathbf{0}. \tag{26}$$

The complex conjugates of the eigenvalues and eigenvectors for $\omega > 0$ are similar to those for $\omega < 0$ and the following relationships hold:

$$\overline{\lambda}_n^{\pm} = \lambda_n^{\mp}, \overline{\widehat{\lambda}}_n^{\pm} = \widehat{\lambda}_n^{\mp}, \widehat{\lambda}_n^{\pm} = -\lambda_n^{\pm}. \tag{27}$$

The eigenvalues and eigenvectors in equations (25) and (26) satisfy the orthogonality requirements [45, 46] as follows:

$$\begin{aligned} (\lambda_n + \lambda_r)\boldsymbol{\psi}_n^T \mathbf{M}\boldsymbol{\psi}_r + \boldsymbol{\psi}_n^T \mathbf{C}\boldsymbol{\psi}_r &= \mathbf{0}, \\ \boldsymbol{\psi}_n^T \mathbf{K}\boldsymbol{\psi}_r - \lambda_n \lambda_r \boldsymbol{\psi}_n^T \mathbf{M}\boldsymbol{\psi}_r &= \mathbf{0}, \end{aligned} \tag{28}$$

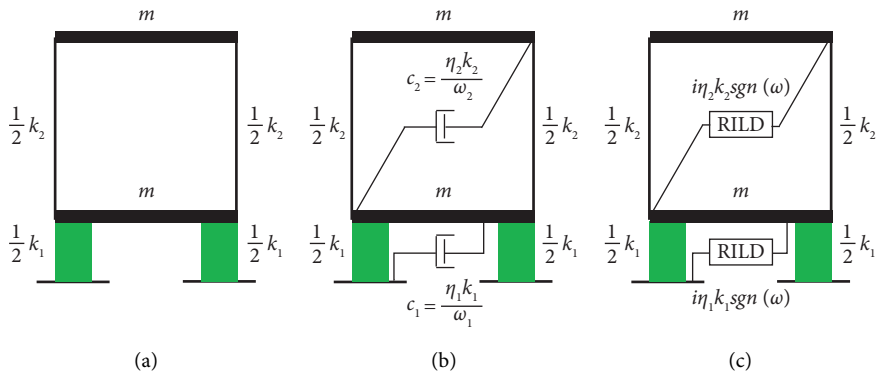

FIGURE 2: Base-isolated two-degree-of-freedom (2DOF) structure: (a) undamped system, (b) linear viscous damping (LVD) system, and (c) rate-independent linear damping (RILD) system.

where ψ_n and ψ_r are the eigenvectors associated with eigenvalues λ_n and λ_r, respectively.

Given the initial condition, the modal parameters (ω_n, ω_{nD}, ζ_n, $S_n^{R\pm}$, and $\widehat{S}_n^{R\pm}$) can be obtained as follows:

$$\begin{aligned}
&\lambda_n^{\pm} = \overline{\lambda}_n^{\mp} = -\zeta_n^R \omega_n^R \pm i\omega_{nD}^R,\ \widehat{\lambda}_n^{\pm} = \overline{\widehat{\lambda}}_n^{\mp} = \zeta_n^R \omega_n^R \mp i\omega_{nD}^R,\\
&\omega_{nD}^R = \omega_n^R \sqrt{1-\left(\zeta_n^R\right)^2},\ \omega_n^R = \left|\lambda_n^{\pm}\right| = \left|\widehat{\lambda}_n^{\pm}\right|,\ \zeta_n^R = -\frac{\mathrm{Re}\left(\lambda_n^{\pm}\right)}{\left|\lambda_n^{\pm}\right|} = \frac{\mathrm{Re}\left(\widehat{\lambda}_n^{\pm}\right)}{\left|\widehat{\lambda}_n^{\pm}\right|},\\
&S_n^{R\pm} = \overline{S}_n^{R\mp} = \frac{\left(\mathbf{v}_n^{\pm}\right)^T \mathbf{L}\mathbf{Z}_0}{\left(\mathbf{v}_n^{\pm}\right)^T \mathbf{L}\mathbf{v}_n^{\pm}} = \frac{\lambda_n^{\pm}\left(\psi_n^{\pm}\right)^T \mathbf{M}\mathbf{X}_0 + \left(\psi_n^{\pm}\right)^T \mathbf{C}\mathbf{X}_0 + \left(\psi_n^{\pm}\right)^T \mathbf{M}\dot{\mathbf{X}}_0}{2\lambda_n^{\pm}\left(\psi_n^{\pm}\right)^T \mathbf{M}\psi_n^{\pm} + \left(\psi_n^{\pm}\right)^T \mathbf{C}\psi_n^{\pm}},\\
&\widehat{S}_n^{R\pm} = \overline{\widehat{S}}_n^{R\mp} = \frac{\left(\widehat{\mathbf{v}}_n^{\pm}\right)^T \mathbf{L}\mathbf{Z}_0}{\left(\widehat{\mathbf{v}}_n^{\pm}\right)^T \mathbf{L}\widehat{\mathbf{v}}_n^{\pm}},
\end{aligned} \tag{29}$$

where superscript R denotes RILD and $\mathbf{Z}_0 = \left[\dot{\mathbf{X}}_0 \ \ \mathbf{X}_0\right]^T$.

The governing equations of motion for the nth mode are decomposed using equation (21) (see Appendix for details).

$$\begin{cases} \left(i\omega - \lambda_n^+\right) Z_n^{R+}(i\omega) - S_n^{R+} = 0, \\ \left(i\omega - \widehat{\lambda}_n^+\right) \widehat{Z}_n^{R+}(i\omega) - \widehat{S}_n^{R+} = 0, \end{cases} \quad (\omega > 0),$$
$$\begin{cases} \left(i\omega - \lambda_n^-\right) Z_n^{R-}(i\omega) - S_n^{R-} = 0, \\ \left(i\omega - \widehat{\lambda}_n^-\right) \widehat{Z}_n^{R-}(i\omega) - \widehat{S}_n^{R-} = 0, \end{cases} \quad (\omega < 0), \tag{30}$$

where $Z_n^{R\pm}(i\omega)$ and $\widehat{Z}_n^{R\pm}(i\omega)$ are the Fourier transforms of modal coordinates $z_n^{R+}(t)$ and $\widehat{z}_n^{R+}(t)$, respectively.

On the basis of the model analysis presented by Chopra [46], and referred to in Appendix, the nth modal response in the time domain is given as follows:

$$\begin{aligned}
\mathbf{X}_n^R(t) = {} & S_n^{R+} \psi_n^+ z_n^{R+}(t) + \widehat{S}_n^{R+} \widehat{\psi}_n^+ \widehat{z}_n^{R+}(t) + S_n^{R-} \psi_n^- z_n^{R-}(t) \\
& + \widehat{S}_n^{R-} \widehat{\psi}_n^- \widehat{z}_n^{R-}(t),
\end{aligned} \tag{31}$$

where

$$z_n^{R+}(t) = \int_0^{+\infty} \frac{1}{i\omega - \lambda_n^+} e^{i\omega t} d\omega,\ \widehat{z}_n^{R+}(t) = \int_0^{+\infty} \frac{1}{i\omega - \widehat{\lambda}_n^+} e^{i\omega t} d\omega,$$
$$z_n^{R-}(t) = \int_{-\infty}^{0} \frac{1}{i\omega - \lambda_n^-} e^{i\omega t} d\omega,\ \widehat{z}_n^{R-}(t) = \int_{-\infty}^{0} \frac{1}{i\omega - \widehat{\lambda}_n^-} e^{i\omega t} d\omega. \tag{32}$$

The methods proposed in [1, 4, 36] can be used to obtain $z_n^{R+}(t)$ and $\widehat{z}_n^{R+}(t)$. $z_n^{R\pm}(t)$ and $\widehat{z}_n^{R\pm}(t)$ are noncausal, i.e., $z_n^{R\pm}(t<0) \neq 0$ and $\widehat{z}_n^{R\mp}(t<0) \neq 0$, respectively.

2.3. Seismic Response. When a multistory building system containing RILD is subjected to impulse ground excitation, that is, $\delta(t)$, we obtain

$$\begin{aligned}
\mathbf{h}_n^R(t) = {} & U_n^{R+} \psi_n^+ z_n^{R+}(t) + \widehat{U}_n^{R+} \widehat{\psi}_n^+ \widehat{z}_n^{R+}(t) + U_n^{R-} \psi_n^- z_n^{R-}(t) \\
& + \widehat{U}_n^{R-} \widehat{\psi}_n^- \widehat{z}_n^{R-}(t),
\end{aligned} \tag{33}$$

where

$$U_n^{R\pm} = \frac{1}{\left(\mathbf{v}_n^{\pm}\right)^T \mathbf{L}\mathbf{v}_n^{\pm}} \left(\mathbf{v}_n^{\pm}\right)^T \mathbf{L} \begin{bmatrix} -\mathbf{r} \\ \mathbf{0} \end{bmatrix} = -\frac{\left(\boldsymbol{\psi}_n^{\pm}\right)^T \mathbf{M}\mathbf{r}}{2\lambda_n^{\pm}\left(\boldsymbol{\psi}_n^{\pm}\right)^T \mathbf{M}\boldsymbol{\psi}_n^{\pm} + \left(\boldsymbol{\psi}_n^{\pm}\right)^T \mathbf{C}\boldsymbol{\psi}_n^{\pm}},$$
$$\widehat{U}_n^{R\pm} = \frac{1}{\left(\widehat{\mathbf{v}}_n^{\pm}\right)^T \mathbf{L}\widehat{\mathbf{v}}_n^{\pm}} \left(\widehat{\mathbf{v}}_n^{\pm}\right)^T \mathbf{L} \begin{bmatrix} -\mathbf{r} \\ \mathbf{0} \end{bmatrix} = -\frac{\left(\widehat{\boldsymbol{\psi}}_n^{\pm}\right)^T \mathbf{M}\mathbf{r}}{2\widehat{\lambda}_n^{\pm}\left(\widehat{\boldsymbol{\psi}}_n^{\pm}\right)^T \mathbf{M}\widehat{\boldsymbol{\psi}}_n^{\pm} + \left(\widehat{\boldsymbol{\psi}}_n^{\pm}\right)^T \mathbf{C}\widehat{\boldsymbol{\psi}}_n^{\pm}}. \tag{34}$$

Note that

$$\overline{z}_n^{R+}(t) = z_n^{R-}(t); \tag{35}$$

similarly,

$$\overline{\widehat{z}}_n^{R+}(t) = \widehat{z}_n^{R-}(t). \tag{36}$$

Using equations (27) and (35), and $U_n^{R\pm}\boldsymbol{\psi}_n^{\pm} = \overline{U}_n^{R\mp}\overline{\boldsymbol{\psi}}_n^{\mp} = -\widehat{U}_n^{R\pm}\widehat{\boldsymbol{\psi}}_n^{\pm} = -\overline{\widehat{U}}_n^{R\mp}\overline{\boldsymbol{\psi}}_n^{\mp}$, the imaginary part of equation (33) vanishes, resulting in

$$\mathbf{X}_n^R(t) = 2\mathrm{Re}\left[U_n^{R+}\boldsymbol{\psi}_n^{+}\left\{z_n^{R+}(t) - \widehat{z}_n^{R+}(t)\right\}\right]. \tag{37}$$

The impulse response in the time domain is given as follows:

$$\mathbf{h}^R(t) = \sum_{n=1}^{N} 2Re\left[U_n^{R+}\boldsymbol{\psi}_n^{+}\left\{z_n^{R+}(t) - \widehat{z}_n^{R+}(t)\right\}\right]. \tag{38}$$

$\boldsymbol{\beta}_n^R$ and $\boldsymbol{\gamma}_n^R$ are defined as follows:

$$2U_n^{R+}\boldsymbol{\psi}_n^{+} = \boldsymbol{\beta}_n^R + i\boldsymbol{\gamma}_n^R, \tag{39}$$

where

$$\boldsymbol{\beta}_n^R = \mathrm{Re}\left(2U_n^{R+}\boldsymbol{\psi}_n^{+}\right), \boldsymbol{\gamma}_n^{R+} = \mathrm{Im}\left(2U_n^{R+}\boldsymbol{\psi}_n^{+}\right). \tag{40}$$

Finally, an alternative expression of the impulse response is given as follows:

$$\begin{aligned} \mathbf{h}^R(t) &= \sum_{n=1}^{N}\left[\boldsymbol{\beta}_n^R z_n^{\mathrm{Re}}(t) - \boldsymbol{\gamma}_n^R z_n^{\mathrm{Im}}(t)\right], \\ z_n^{\mathrm{Re}}(t) &= \mathrm{Re}\left[z_n^{R+}(t) - \widehat{z}_n^{R+}(t)\right], \\ z_n^{\mathrm{Im}}(t) &= \mathrm{Im}\left[z_n^{R+}(t) - \widehat{z}_n^{R+}(t)\right]. \end{aligned} \tag{41}$$

The impulse-response functions of an LVD system with eigenvalue $\lambda_n^{R+} = -\zeta_n^R\omega_n^R + i\omega_{nD}^R$ are defined as follows:

$$\widetilde{h}_n^R(t) = \begin{cases} 0, & (t<0), \\ -\dfrac{1}{\omega_{nD}^R} e^{-\zeta_n^R\omega_n^R t}\sin\omega_{nD}^R t, & (t\geq 0). \end{cases} \tag{42}$$

Then,

$$\dot{\widetilde{h}}_n^R(t) \simeq \begin{cases} 0, & (t<0), \\ -e^{-\zeta_n^R\omega_n^R t}\cos\omega_{nD}^R t - \zeta_n^R\omega_n^R\widetilde{h}_n^R(t), & (t\geq 0). \end{cases} \tag{43}$$

Therefore, the causal approximation of the impulse response is given as follows:

$$\mathbf{h}^R(t) \simeq \widetilde{\mathbf{h}}^R(t) = -\sum_{n=1}^{N}\left[\boldsymbol{\alpha}_n^R\omega_n^R\widetilde{h}_n^R(t) + \boldsymbol{\beta}_n^R\dot{\widetilde{h}}_n^R(t)\right], \boldsymbol{\alpha}_n^R = \zeta_n^R\boldsymbol{\beta}_n^R - \sqrt{1-\left(\zeta_n^R\right)^2}\boldsymbol{\gamma}_n^R. \tag{44}$$

Employing Duhamel's integral, the causally approximated displacement response of the noncausal RILD system is given as follows:

$$\mathbf{X}^R(t) \simeq \widetilde{\mathbf{X}}^R(t) = \int_{-\infty}^{+\infty} \ddot{x}_g(\tau)\widetilde{\mathbf{h}}^R(t-\tau)d\tau, \tag{45}$$

where $\widetilde{\mathbf{h}}^R(t)$ can be obtained using equation (44), resulting in

$$\widetilde{\mathbf{X}}^R(t) = -\sum_{n=1}^{N}\left[\boldsymbol{\alpha}_n^R\omega_n^R D_n^R(t) + \boldsymbol{\beta}_n^R\dot{D}_n^R(t)\right], \tag{46}$$

where

$$\begin{aligned} D_n^R(t) &= \int_0^t \ddot{x}_g(\tau)\widetilde{h}_n^R(t-\tau)d\tau, \\ \dot{D}_n^R(t) &= \int_0^t \ddot{x}_g(\tau)\dot{\widetilde{h}}_n^R(t-\tau)d\tau. \end{aligned} \tag{47}$$

This enabled us to use response spectrum approaches to obtain the maximum dynamic responses of systems containing proportionally or nonproportionally distributed RILD.

3. Numerical Verification

3.1. Structural Model. A single-story base-isolated shear building serves as a structural model that represents low-frequency structures. Following the Japanese design code of the base-isolation structure [59], the fundamental natural period of the base-isolated system when undamped and the superstructure is assumed to be a rigid body is designed to be approximately 4.0 s. The loss factors were $\eta_1 = 0.40$ and $\eta_2 = 0.04$. The stiffness of the second floor was changed to ensure that the second natural period of the 2DOF systems was in the range of 0.2–1.2 s. Table 1 summarizes the parameters of the 2DOF systems.

3.2. Results of Impulse-Response Precursors. Using the data presented in Table 1 and equation (10), we calculated the impulse response of the RILD system. As indicated in the literature [38, 39, 57], an impulsive reaction is maximum at $t = 0$ in the nonpositive time region. Therefore, it is only necessary to set $t = 0$ to obtain the maximum impulse-response precursor (i.e., maximum absolute value).

Table 2 presents the maximum impulse-response precursors in the nonpositive time region ($IRP_{non-positive}$), maximum values of impulse responses in the positive time region ($IRP_{positive}$), and their ratios ($IRP_{non-positive}/IRP_{positive}$). The IRP values of the undamped and LVD systems are both zero and not shown here.

As shown in Table 2, the ratios of $IRP_{non-positive}/IRP_{positive}$ are approximately 0.2 for the 2DOF systems. The maximum impulse response of the isolation layer is at time $t = 0$ in the nonpositive time region. However, the maximum impulse response of the roof floor moved to negative around $t = 0$, and the roof floor responded behind the isolation layer in the positive time region as the upper structure became softer owing to the modal characteristics.

3.3. Earthquake Response

3.3.1. Input Ground Motion. Six earthquake records [60, 61] were used for modal analysis. Low-frequency records included Sakishima, Tohoku, Hachinohe, and Tomakomai. The essential ground motion information is listed in Table 3. Figures 3 and 4 show the time histories and spectral features, respectively.

3.3.2. Dynamic Responses. The 2DOF base-isolated systems were used as structural models to evaluate the performance of the proposed modal decomposition technique. The results of the RILD systems obtained from the fast Fourier transform (FFT) [31] were compared with those obtained using the proposed approximation method discussed before. In addition, the dynamic responses of LVD systems with identical loss factors are presented in this section.

Figure 5 shows a comparison of the peak relative displacement values of the isolation layer. The results show that compared with the FFT approach, the proposed method can provide an excellent approximation. When the superstructure changes from rigid to soft, the errors between the results obtained from the approximated method and FFT are acceptable and in the range of −11.11%–3.26%. Furthermore, the displacement responses can be controlled similarly using the RILD and LVD devices, and the RILD device is only slightly compromised in some cases.

Figure 6 shows the peak relative velocity values of the isolator. No discernible differences were observed between RILD and LVD groups. The errors between the approximated method and FFT analysis were in the range of −6.44%–6.68%, indicating that relative velocities of the 2DOF system were correctly predicted by the proposed method. However, the proposed method is somewhat compromised when the second natural period of the structure reaches the predominant frequency of the ground motions. For instance, when the second period of the 2DOF system was 0.8 s, close to the dominant frequency of the Kobe record (1.45 Hz), the error between the approximated and FFT methods was up to 6.68%, the largest among the six ground motions.

Figure 7 shows the peak roof floor acceleration values of the 2DOF systems. Except for the Tomakomai and Sakishima records, the LVD system floor response accelerations were significantly greater than those with RILD. The errors between the proposed and FFT methods were small and in the range of −8.24%–1.91%. The largest error (−8.24%) was observed in the Hachinohe record, when the second natural period was 1.2 s. The second largest error occurred in the Kobe record when the second natural period was 0.8 s, which was relatively close to the dominant frequency of the ground motion.

Consequently, the proposed causal method offers an excellent approximation of the peak response of the structure, thereby providing a new approach for conducting time-domain analysis of noncausal RILD structures. The aforementioned observation indicates that the differences between the results of FFT and proposed method tend to increase when the dominant frequency of the ground motions near the second natural period of the 2DOF systems. This was because of the excitation of the high mode of the structure by the ground motion, exacerbating the inefficiency of the proposed method.

3.3.3. Responses of Separated Modes. To reveal the differences between the single-mode responses of the 2DOF nonproportionally distributed RILD and LVD systems, we obtained the separated-mode responses of the RILD system using the proposed modal decomposition approach and compared to those of the LVD system.

Figure 8 shows the displacement responses of the RILD and LVD systems belonging to the first and second modes. The modal displacements of the first mode of both systems were almost identical in all cases. Because the vibration of the base-isolated structure was dominated in the first mode, both systems exhibited similar displacement responses. In the second mode, the RILD system had smaller displacements compared to the LVD system for all selected earthquakes. The differences between the modal displacement responses of the second mode increased as the

Table 1: Parameters of the two-degree-of-freedom (2DOF) systems.

Cases	Floor	Mass (tons)	Stiffness (kN/m)	LVD (kN · s/m)	RILD (kN/m)	First natural period (s)	Second natural period (s)
1	2	1.0	492.00	0.6266	19.6800i	3.99	0.20
	1	1.0	4.97	1.2632	1.9896i		
2	2	1.0	122.12	0.3110	4.8848i	4.00	0.40
	1	1.0	4.97	1.2681	1.9896i		
3	2	1.0	53.55	0.2046	2.4120i	4.03	0.60
	1	1.0	4.97	1.2766	1.9896i		
4	2	1.0	29.55	0.1505	1.1820i	4.07	0.80
	1	1.0	4.97	1.2890	1.9896i		
5	2	1.0	18.41	0.1172	0.7365i	4.13	1.00
	1	1.0	4.97	1.3063	1.9896i		
6	2	1.0	12.34	0.0943	0.4936i	4.20	1.20
	1	1.0	4.97	1.3297	1.9896i		

Table 2: Impulse responses of the rate-independent linear damping (RILD) systems.

Cases	Floor	$IRP_{non-positive}$ (m)	$IRP_{positive}$ (m)	$IRP_{non-positive}/IRP_{positive}$
1	2	−0.0729	0.3669	−0.1988
	1	−0.0725	0.3645	−0.1989
2	2	−0.0739	0.3700	−0.1998
	1	−0.0722	0.3652	−0.1976
3	2	−0.0758	0.3844	−0.1971
	1	−0.0714	0.3598	−0.1985
4	2	−0.0787	0.3755	−0.2097
	1	−0.0702	0.3749	−0.1872
5	2	−0.0831	0.4175	−0.1990
	1	−0.0683	0.3674	−0.1858
6	2	−0.0891	0.4600	−0.1937
	1	−0.0700	0.3362	−0.2083

Table 3: Earthquake records (North-South component).

Records	Duration (s)	Magnitude (Mw)	Peak ground acceleration (g)	Date of occurrence
El Centro	53.74	6.9	0.342	1940/05/18
Tohoku	321.03	9.0	0.333	2011/03/11
Kobe	19.98	6.9	0.818	1995/01/17
Tomakomai	290.00	8.0	0.087	2003/09/26
Hachinohe	234.00	7.9	0.230	1968/05/16
Sakishima	220.00	9.0	0.034	2011/03/11

superstructure softened, thus demonstrating the benefits of RILD in controlling high-mode responses of low-frequency structures.

Figure 9 shows the modal velocity responses. The results for the first mode did not show any significant differences. As the second natural period of the 2DOF systems increased, the velocity responses of the first mode decreased for all selected ground motions. In contrast, the velocity response of the second mode increased as the superstructure became softer. Furthermore, the difference between the velocity responses of the second mode of both systems was greater than those of the first mode because RILD outperforms LVD in controlling higher mode responses. Furthermore, the velocity response for the second mode in the Kobe record was significantly larger than that of the other five earthquake records, owing to the large number of high-frequency components.

Figure 10 shows the modal acceleration responses. The acceleration responses of both the first and second modes of the system containing RILD were smaller than those of the system containing LVD. The acceleration responses of the first mode indicated that the RILD device exhibited a constant performance in controlling the floor acceleration responses and was generally unaffected by changes in the

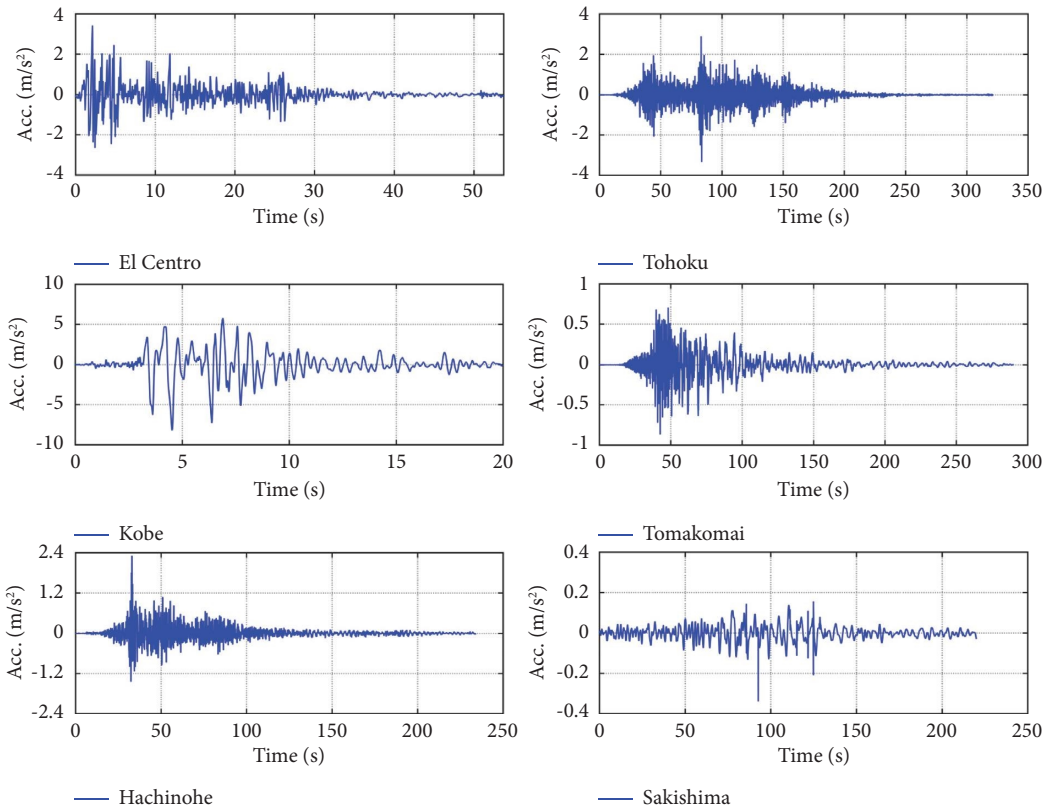

Figure 3: Time histories of earthquake records.

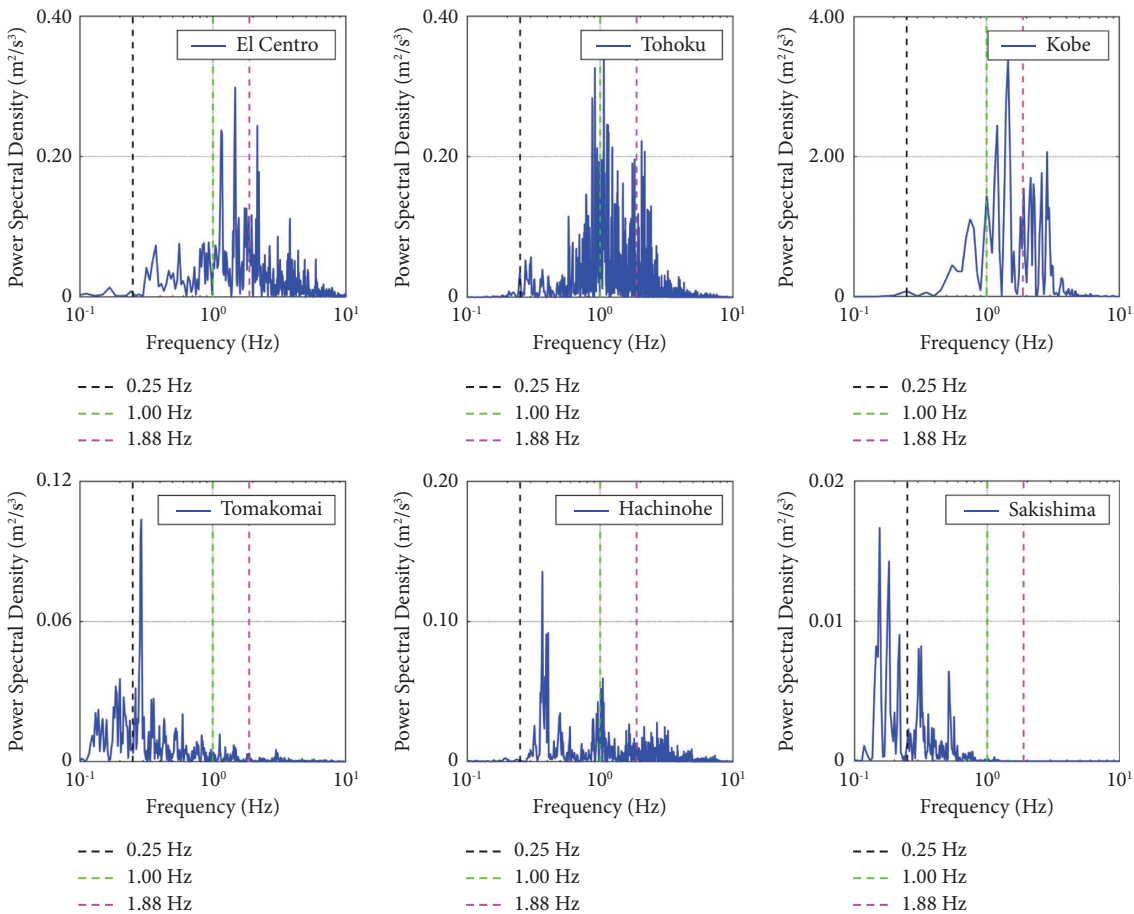

Figure 4: Power spectral density (PSD).

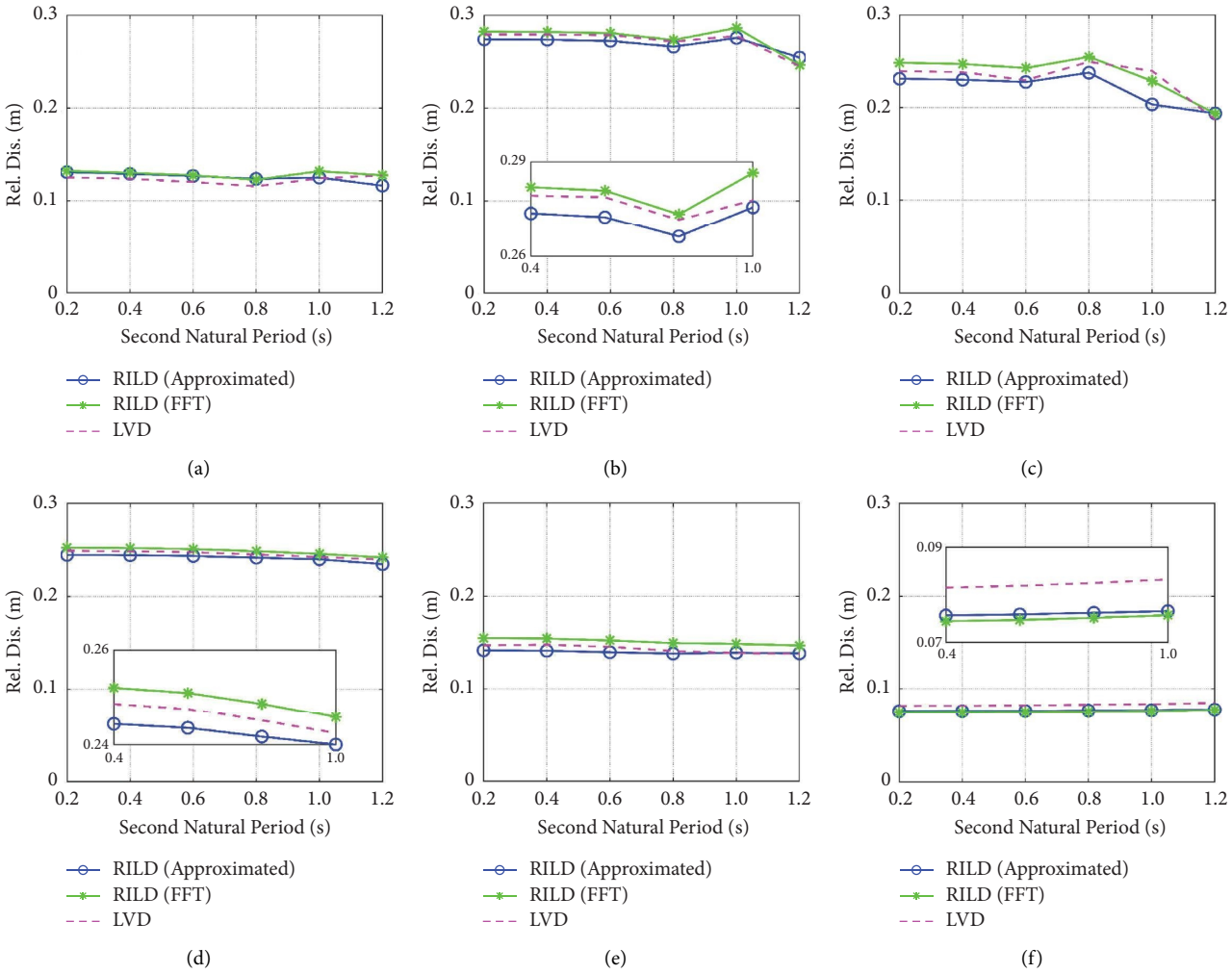

Figure 5: Peak relative displacement values of the isolator. (a) El Centro. (b) Tohoku. (c) Kobe. (d) Tomakomai. (e) Hachinohe. (f) Sakishima.

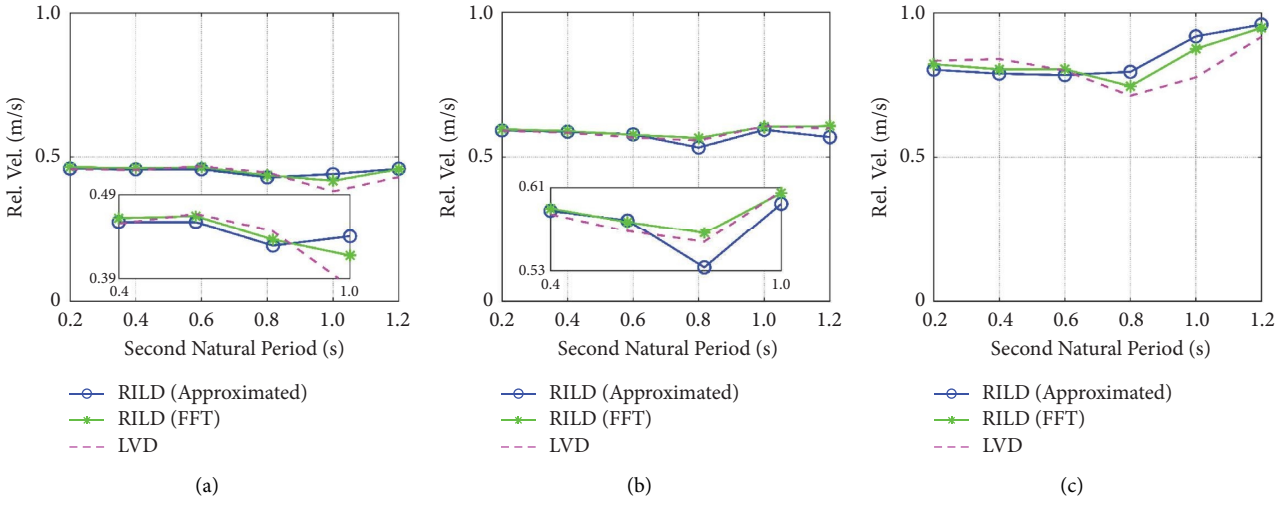

Figure 6: Continued.

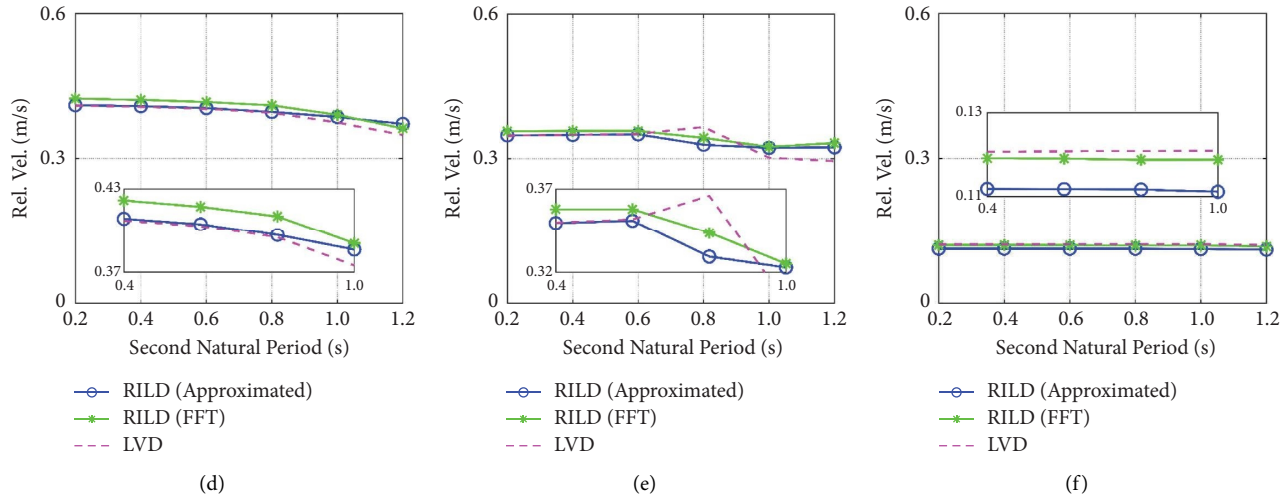

FIGURE 6: Peak relative velocity values of the isolator. (a) El Centro. (b) Tohoku. (c) Kobe. (d) Tomakomai. (e) Hachinohe. (f) Sakishima.

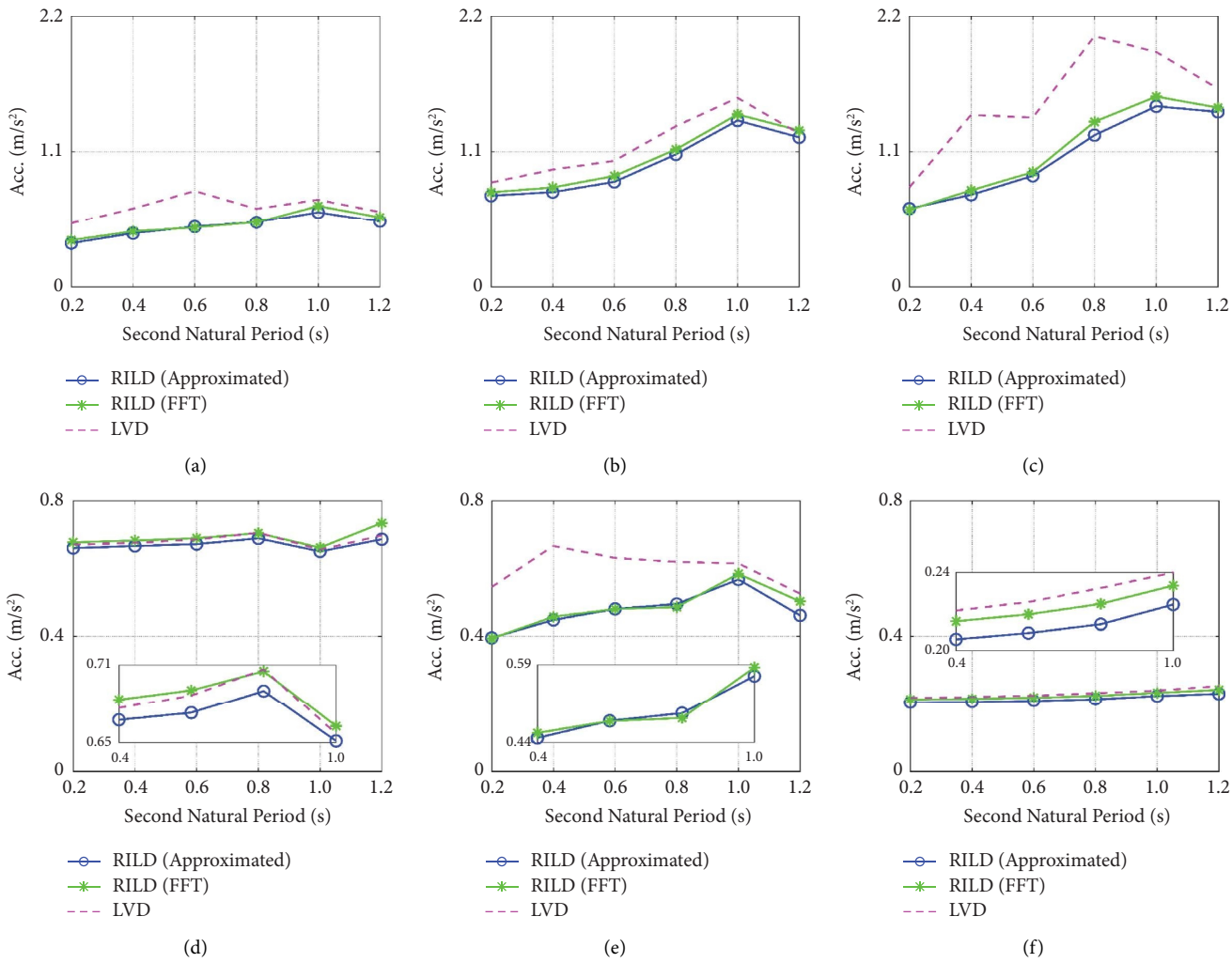

FIGURE 7: Peak roof-floor response acceleration values. (a) El Centro. (b) Tohoku. (c) Kobe. (d) Tomakomai. (e) Hachinohe. (f) Sakishima.

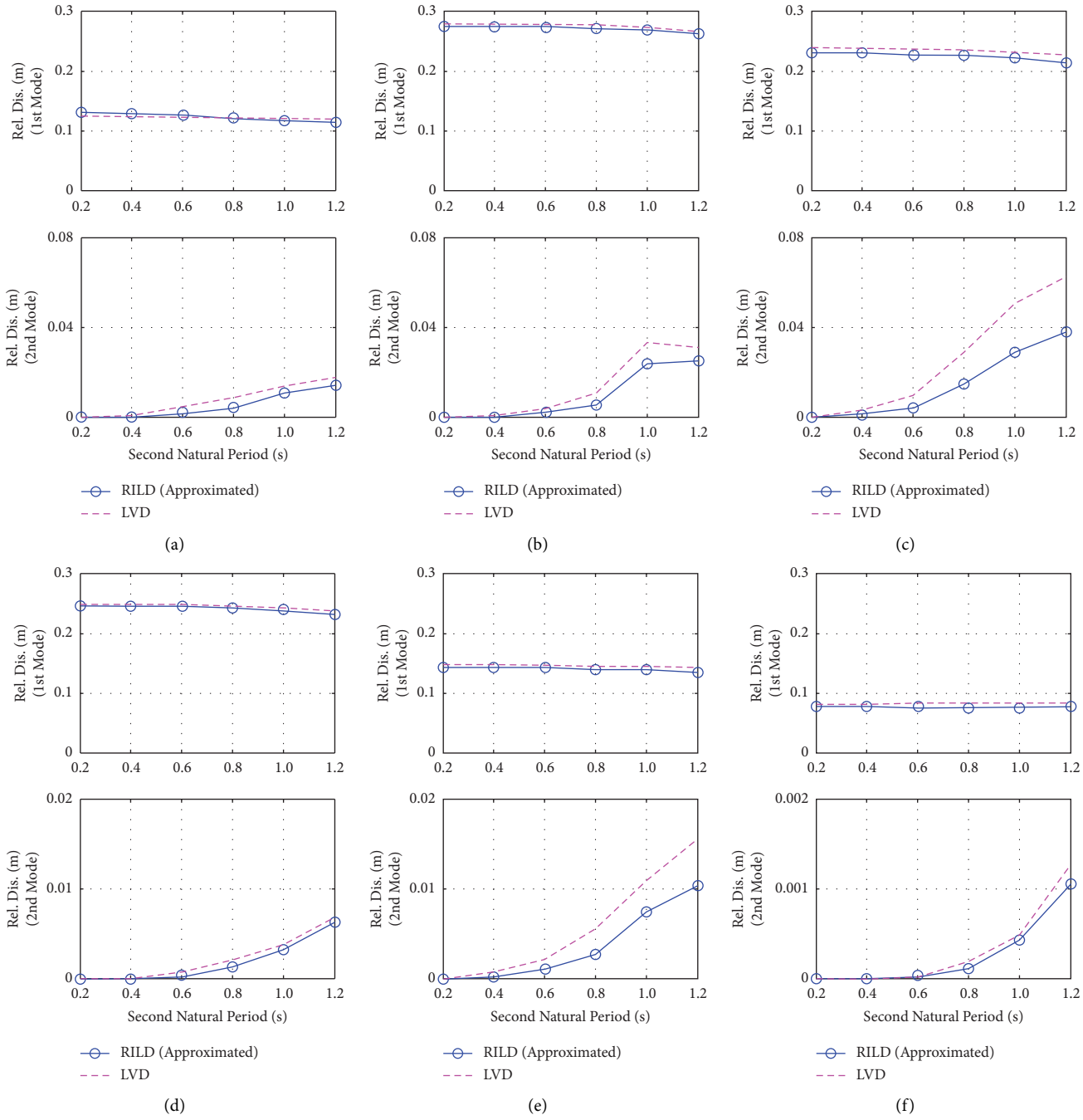

Figure 8: Displacement responses of separated modes. (a) El Centro. (b) Tohoku. (c) Kobe. (d) Tomakomai. (e) Hachinohe. (f) Sakishima.

superstructure stiffness. However, the impact of control on the second mode of both systems differed, considering the second natural period of the 2DOF systems increased from 0.2 s to 1.2 s.

For the Kobe record, the second mode played a more significant role, thereby indicating that the response acceleration was dominated by the second mode. For the Sakishima record, the amplitude of the acceleration responses of the second mode was very small, owing to its inherent characteristics.

Table 4 lists the modal damping ratios of the 2DOF systems containing RILD and LVD. Evidently, the damping ratios for the first mode decrease as the second natural period increases. However, the damping ratios of the second

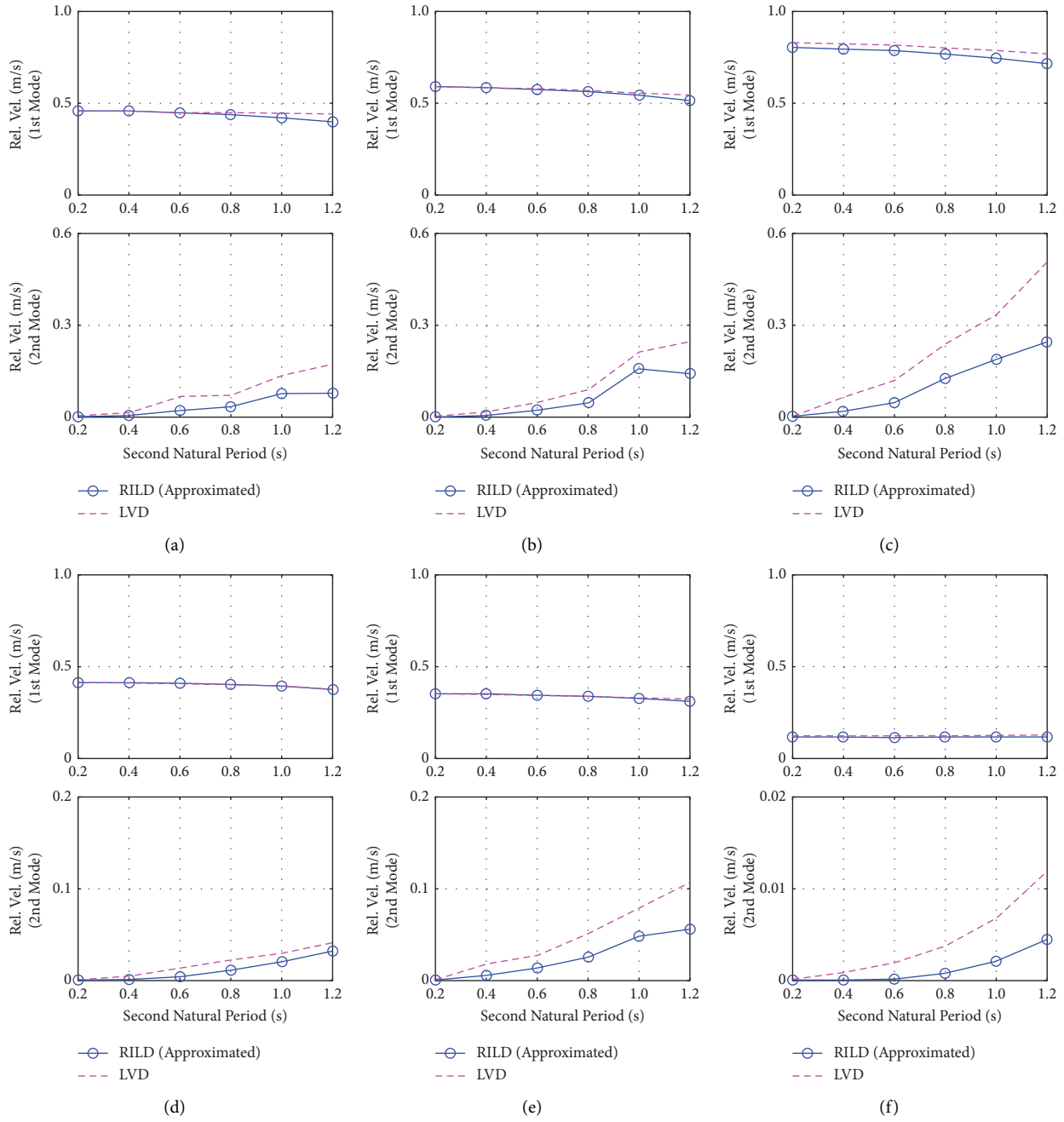

Figure 9: Velocity responses of separated modes. (a) El Centro. (b) Tohoku. (c) Kobe. (d) Tomakomai. (e) Hachinohe. (f) Sakishima.

mode increased with the period. In addition, the modal damping ratios of the RILD system were lower than those of the LVD system. Larger damping ratios would compromise the structural acceleration responses. Therefore, although the loss factors of the RILD and LVD devices were identical, modal acceleration responses of the RILD systems were lesser; this was caused by the differences in modal damping ratios.

3.4. Application in a High-Rise Building. To further investigate the feasibility of the proposed modal decomposition method for a system with more degrees of freedom, a 10-story shear-flexural building [62] (the parameters of which are listed in Table 5) is utilized as a benchmark example, and Table 6 shows the periods and frequencies of this undamped model.

3.4.1. Displacement Responses of the Multistory Structure. The records of Kobe and Tomakomai were used to investigate the performance of the developed modal analysis method. Figure 11 shows the relative displacements of the isolator and 5^{th} and 10^{th} floors. The proposed method obtained satisfactory results in contrast to the frequency-domain analysis. Furthermore, the peak relative

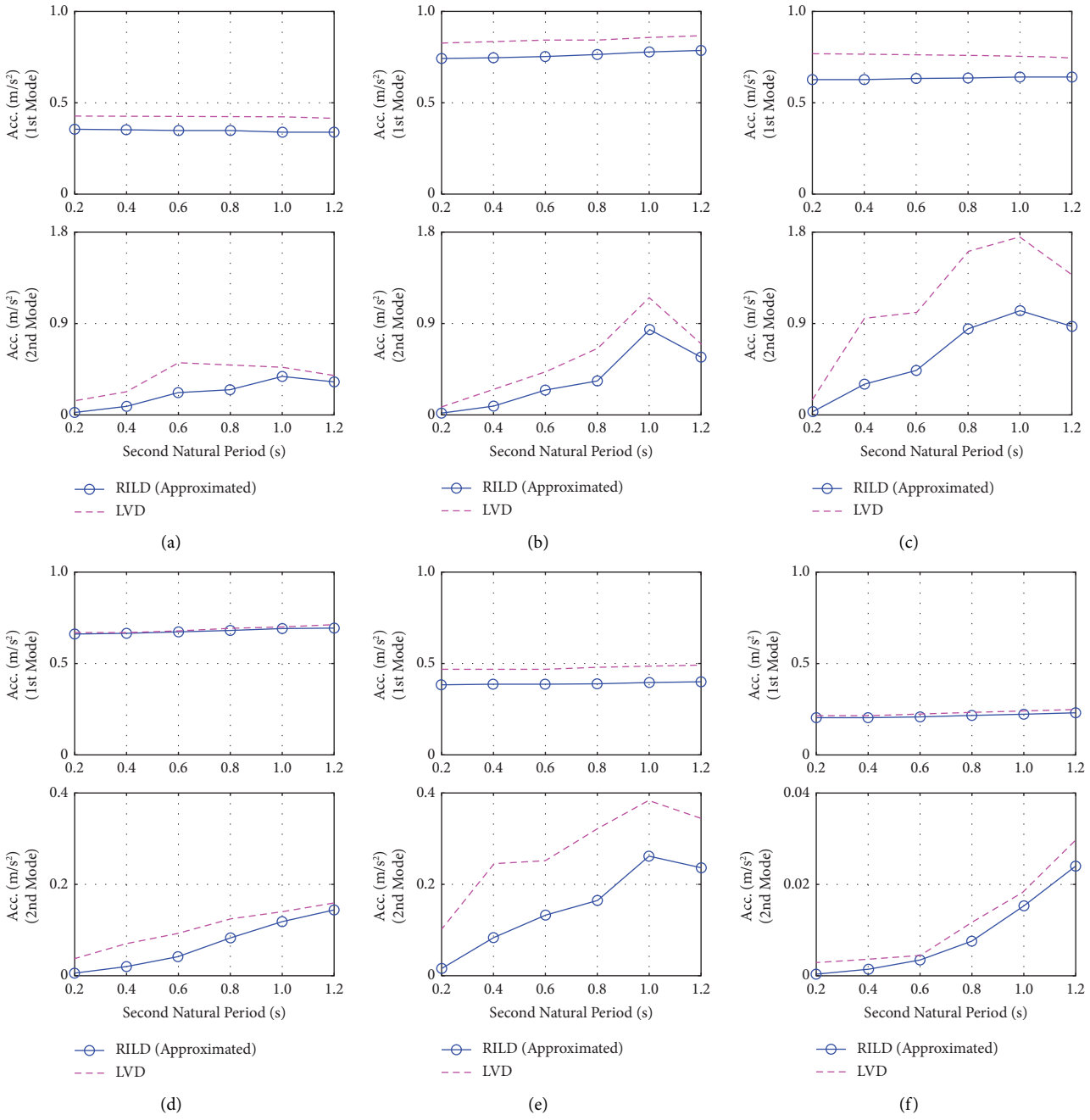

Figure 10: Acceleration responses of separated modes. (a) El Centro. (b) Tohoku. (c) Kobe. (d) Tomakomai. (e) Hachinohe. (f) Sakishima.

Table 4: Modal damping ratios of the two-degree-of-freedom (2DOF) systems containing rate-independent linear damping (RILD) and conventional linear viscous damping (LVD) (%).

Second natural period (s)		0.2	0.4	0.6	0.8	1.0	1.2
1st mode	RILD	18.87	18.73	18.49	18.14	17.65	16.99
	LVD	19.95	19.81	19.57	19.20	18.70	18.01
2nd mode	RILD	2.04	2.18	2.43	2.78	3.28	3.95
	LVD	3.01	4.04	5.14	6.36	7.75	9.38

Table 5: Detailed information on the analytical model.

Story	Primary structure		
	Mass (tons)	Stiffness (kN/m)	Height (m)
10	875	158550	4.0
9	649	180110	4.0
8	656	220250	4.0
7	660	244790	4.0
6	667	291890	4.0
5	670	306160	4.0
4	676	328260	4.0
3	680	383020	4.0
2	682	383550	4.0
1 (isolation layer)	700	20297	2.0

Table 6: Periods and frequencies of the multistory model.

Mode	1st	2nd	3rd	4th	5th	6th	7th	8th	9th	10th
Periods (s)	4.00	1.00	0.53	0.36	0.28	0.23	0.20	0.18	0.16	0.14
Natural frequencies (Hz)	0.25	1.00	1.88	2.77	3.62	4.31	4.98	5.56	6.25	6.98
Circular frequencies (rad/s)	1.57	6.29	11.83	17.42	22.74	27.10	31.28	34.95	39.27	43.83

displacements of the three selected floors obtained by the two different methods matched very well, and the discrepancy varied in the ranges of (2.22%–4.89%) and (5.20%–6.38%) for the Kobe and Tomakomai records, respectively.

3.4.2. Modal Relative Displacements. Figure 12 shows a comparison of the relative displacements of the isolation layer of the separated modes of the two systems. Only the first three modes are shown here to save space. Evidently, there is no significant difference between the first modes of the two damped structures. When the second and third modes were considered for both the selected records, the relative displacements of the LVD system were much higher.

3.4.3. Modal Relative Velocities. Figure 13 shows the relative modal velocities. The velocity responses of the LVD system for the first mode were almost identical to those of the RILD systems. For the second- and third-order modes, though, the velocities of the LVD system were significantly higher.

3.4.4. Modal Accelerations. Figure 14 shows the modal acceleration responses of the two damping systems to investigate the actual control effects of the LVD and RILD devices. The results clearly demonstrate that the LVD system experienced a larger acceleration for the first three modes, thereby indicating the efficiency of the RILD device in reducing the acceleration responses, especially for the high modes of the multistory structure.

3.4.5. Modal Damping Force. Figure 15 shows the normalized damping forces of the two damping systems (F_d is the modal damping force and m is the modal mass). The results show that the RILD and LVD provide almost identical damping forces in the isolation layer for the first mode. However, the generated control force of LVD is much larger than that of RILD in the second and third modes, thereby indicating that maintaining a lower control force is an advantage of RILD.

3.4.6. Modal Interstory Drift. Figure 16 shows a comparison of the modal interstory drifts. RILD effectively mitigated the interstory drift of the first three modes and the total responses in the Kobe and Tomakomai records. The second mode was dominant in the Kobe record which contained many high-frequency components. However, the first mode was more significant in the case of low-frequency ground motion, that is, the Tomakomai record.

4. Experimental Verification

4.1. Causal Realization of RILD. To overcome the noncausality of RILD, Keivan et al. [25, 26] proposed a digital filter to approximate the behavior of RILD (i.e., to approximate the Hilbert transform (isgn(ω)) using the filter). The filter takes the following form:

$$H_{\mathrm{C}}(\omega) = \frac{i\omega - \omega_1}{i\omega + \omega_1}. \tag{48}$$

Therefore, the damping force of RILD is causally realized by

$$F_{\mathrm{R}} \simeq F_{\mathrm{C}} = \eta k \frac{i\omega - \omega_1}{i\omega + \omega_1} X_{\mathrm{C}}(i\omega). \tag{49}$$

Equation (49) represents a parallel combination of the negative stiffness ($k_N = -\eta k$) and Maxwell elements (constructed by connecting a stiffness unit $k_M = 2\eta k$ and a viscous damper $c_M = 2\eta k/\omega_1$ in series) as follows:

$$F_{\mathrm{C}} = \left(-\eta k + 2\eta k \frac{i\omega}{i\omega + \omega_1} \right) X_{\mathrm{C}}. \tag{50}$$

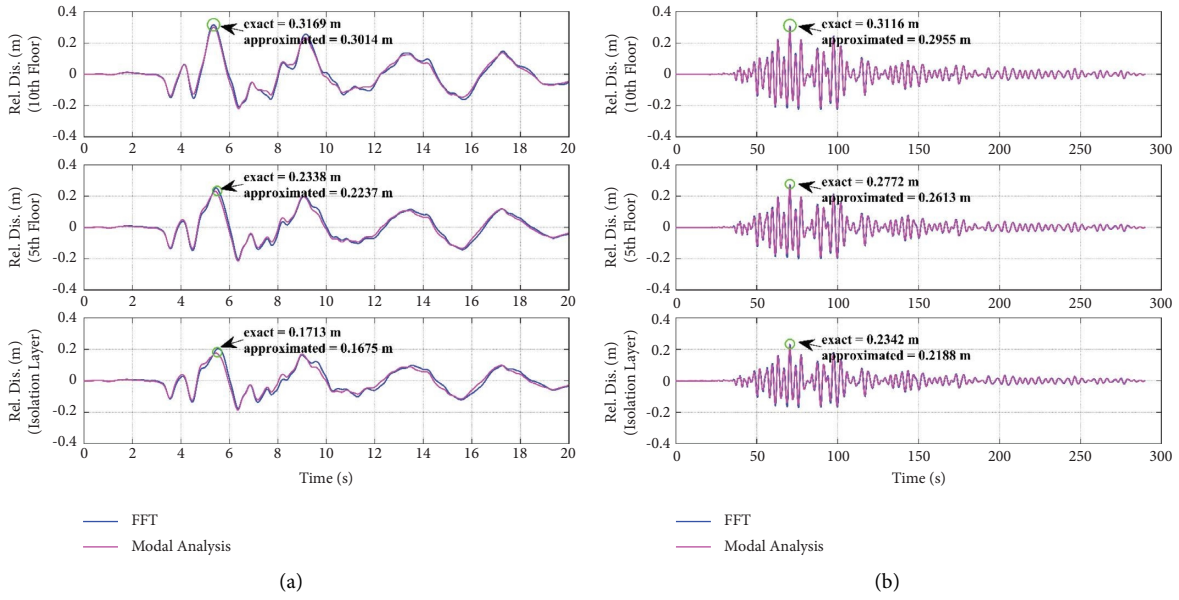

Figure 11: Relative displacements of multistory structure. (a) Kobe. (b) Tomakomai.

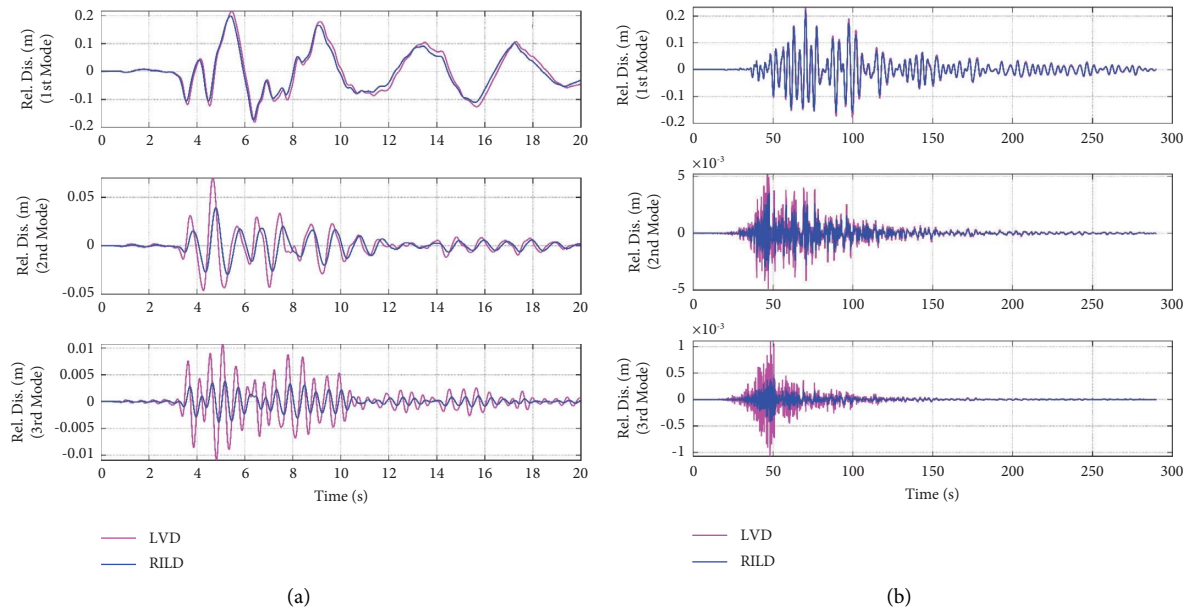

Figure 12: Relative displacements of the isolator of separated modes. (a) Kobe. (b) Tomakomai.

4.2. Experimental Setup. A coil spring unit and oil damper were designed and fabricated to build a Maxwell-type damper. Their characteristics were identified experimentally, as shown in Figure 17. The stiffness and maximum frictional force of the coil spring were identified as 14.50 kN/m and 163.91N, respectively. The damping coefficient of the oil damper is 12.09 kN·s/m.

A ten-story base-isolated building was used as the analytical model, and its parameters are shown in Figure 18. The device constructed using the negative stiffness and Maxwell-type damper is called causal rate-independent linear damping (CRILD) in this section. A viscous damping element, c_c (whose value is 1.83 kN·s/m), was connected in parallel to k_M so as to consider the inherent friction force of the spring element.

Considering the labor and time costs, the real-time hybrid simulation (RTHS) [63, 64] was adopted other than conventional shaking table testing. The entire system was divided into numerical and physical domains. In the physical domain, only the Maxwell-type damper was placed on the shaking table, and the control displacement was applied using actuators, as shown in Figure 19. The remainder of the system was constructed using MATLAB/Simulink. A negative stiffness ($k_N = -7.25 \times 1000 = -7250$ kN/m)

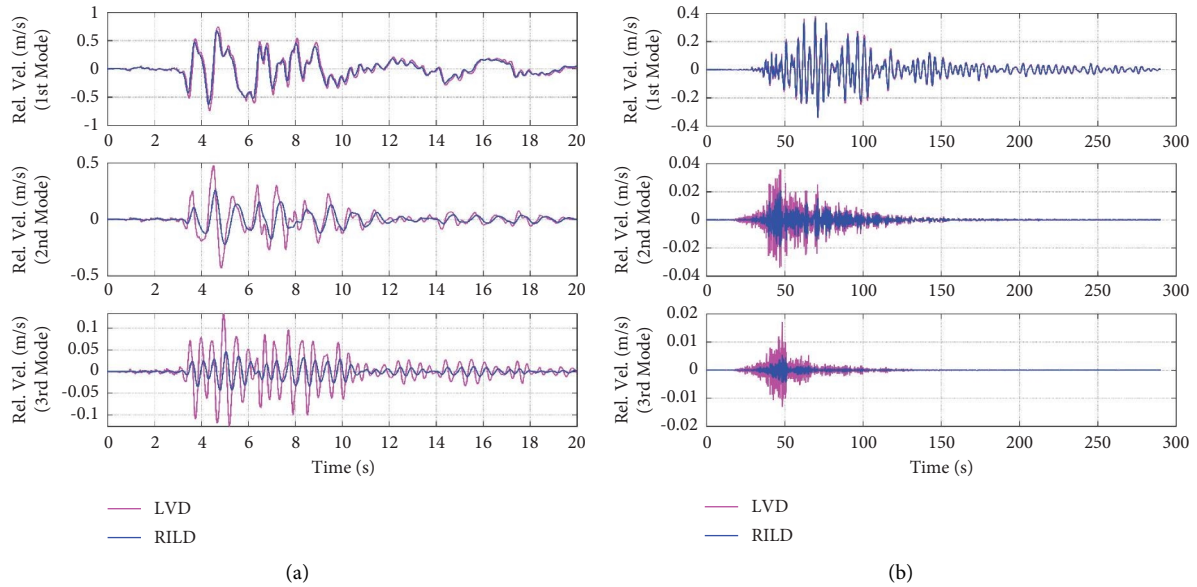

Figure 13: Relative velocities of separated modes. (a) Kobe. (b) Tomakomai.

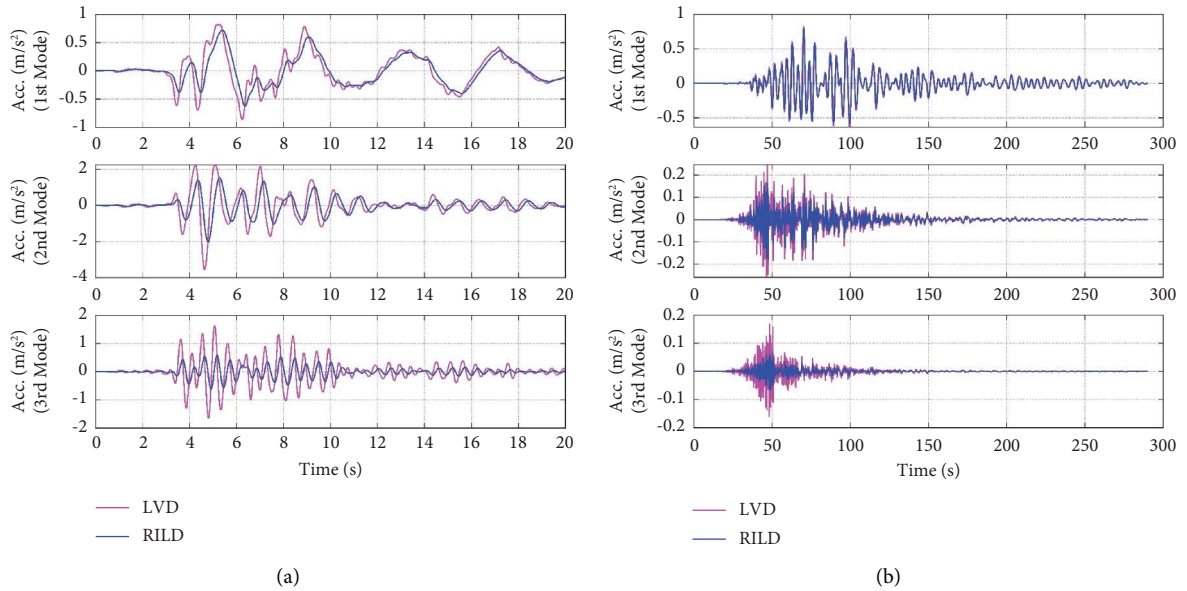

Figure 14: Modal accelerations of separated modes. (a) Kobe. (b) Tomakomai.

in the CRILD device was achieved by reducing the stiffness of the isolator in the numerical domain rather than using physical devices.

4.3. Experimental Results. Kobe and Tomakomai records were utilized in the RTHS, with scale factors of 45% and 30%, respectively. Because the Maxwell-type damper was small-scale and multiple dampers were usually installed in an actual building, the target damping ratio ($\xi = \eta/2 = 0.20$) was achieved by multiplying the measured damping force of the Maxwell-type damper by 1000 and providing feedback to the RTHS loop.

Figures 20 and 21 show the power spectral density (PSD) of the relative displacement, relative velocity, absolute acceleration, and damping force of the isolation layer of the ten-story structure equipped with the CRILD, LVD, and ideal RILD devices. In the selected records, the ideal RILD and LVD systems exhibited similar displacement and velocity responses. Regarding the structure incorporated with the CRILD device, the experimental results showed that the CRILD system experienced a smaller acceleration response than the LVD system, and the damping force generated by the CRILD was lower than that of the LVD. In the high-frequency-dominant Kobe record, both the experimental and numerical results demonstrated that the CRILD and

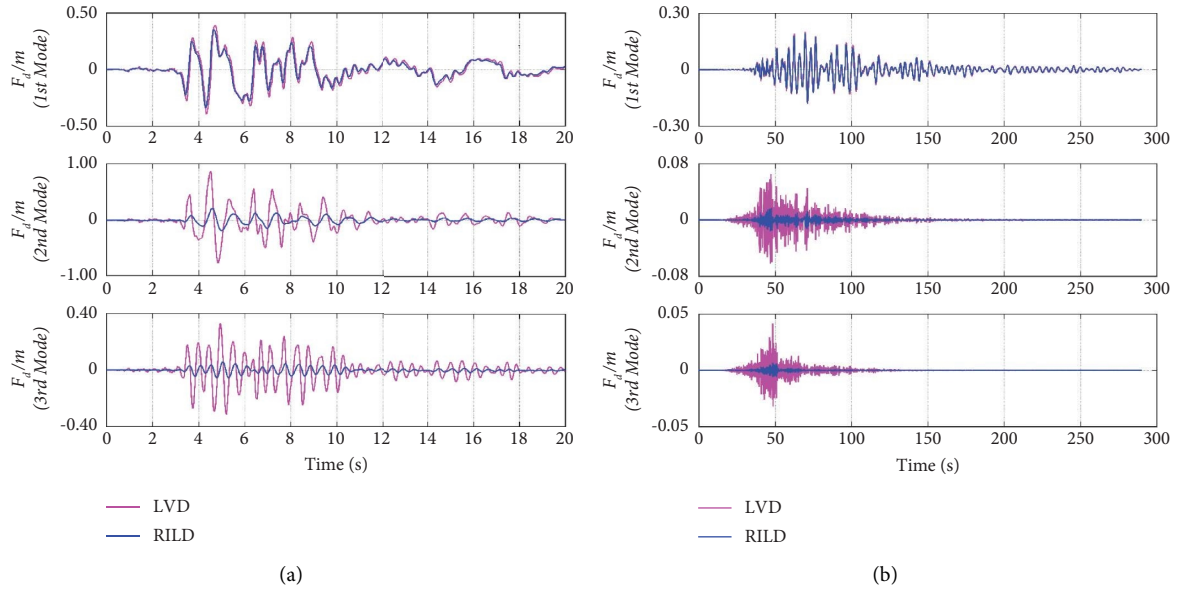

Figure 15: Modal normalized damping force of separated modes. (a) Kobe. (b) Tomakomai.

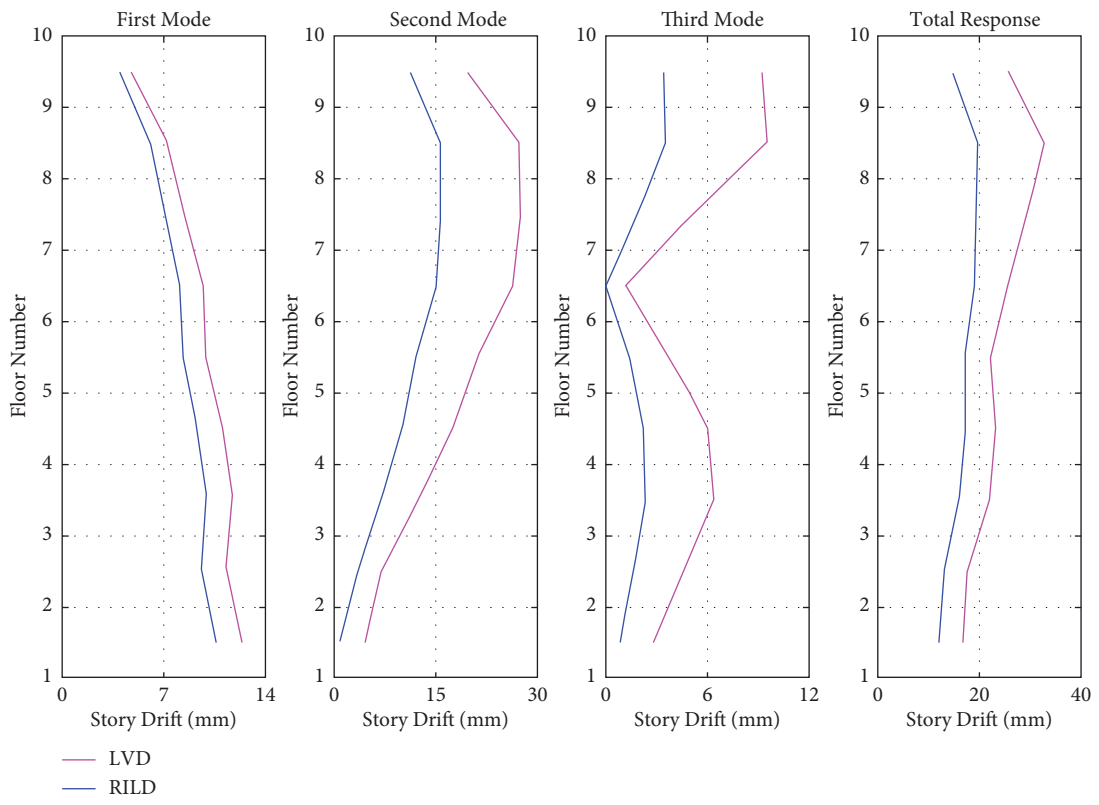

Figure 16: Continued.

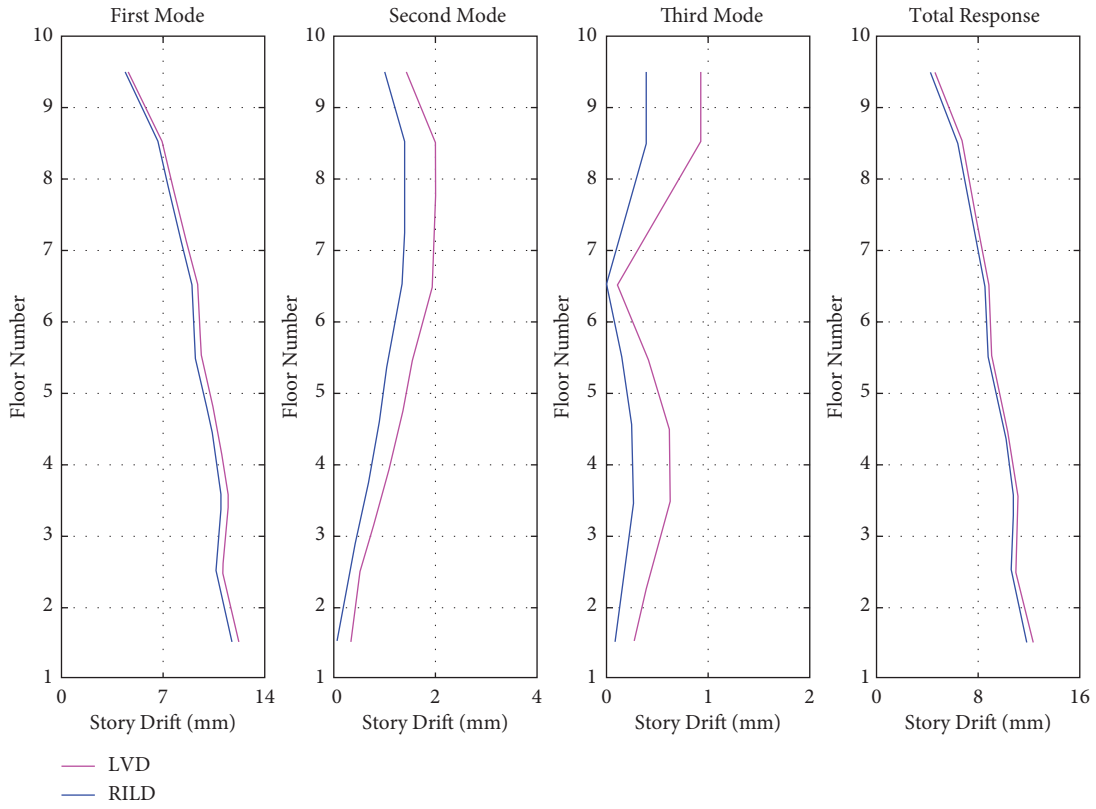

(b)

Figure 16: Modal interstory drift. (a) Kobe. (b) Tomakomai.

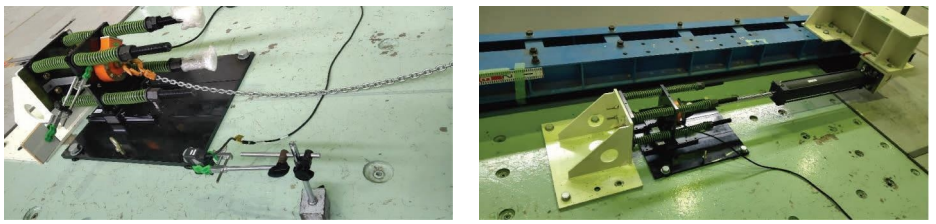

(a) (b)

Figure 17: Identification of specimens. (a) Coil spring. (b) Maxwell-type damper.

ideal RILD outperformed the LVD in reducing the acceleration response and damping force, particularly in the high modes of high-rise buildings. This observation is consistent with the results presented in Section 3.4.

Because the Tomakomai record has a large number of low-frequency components and its duration exceeds 300 s, environmental and electric noises have some influence on the results in the low-frequency region, as shown in Figure 21. Overall, the RTHS proved the feasibility of realizing an ideal RILD using the proposed CRILD device and demonstrated that RILD-based devices can provide a promising approach to mitigate the acceleration responses in the high modes of a high-rise building and maintain a lower damping force than conventional LVD devices can in the high-frequency region.

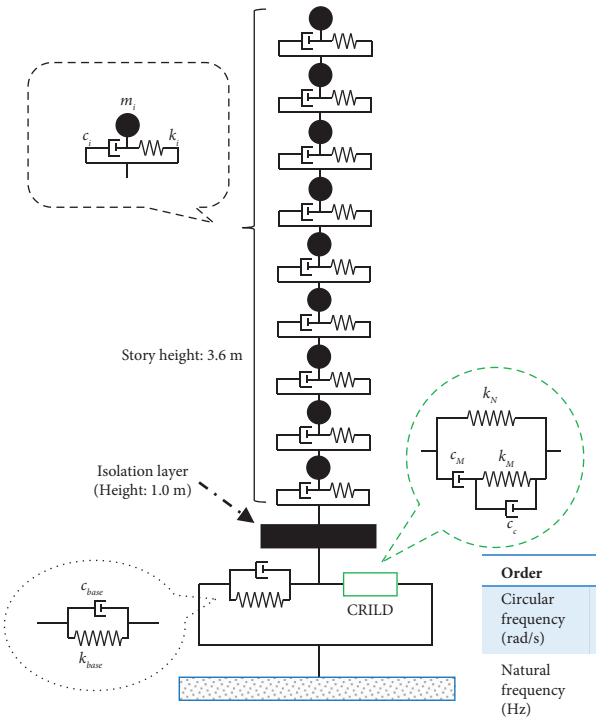

Story number	Mass (ton)	Linear stiffness (kN/m)	Inherent damping (kN·s/m)
9	1260	131200	7590
8	1260	131200	7590
7	1260	131200	7590
6	1260	131200	7590
5	1260	131200	7590
4	1260	131200	7590
3	1260	131200	7590
2	1260	131200	7590
1	1260	131200	7590
Isolation layer	1260	18130	0

Order	1	2	3	4	5	6	7	8	9	10
Circular frequency (rad/s)	1.19	10.24	19.98	29.34	37.95	45.68	52.21	57.49	61.39	63.77
Natural frequency (Hz)	0.19	1.63	3.18	4.67	6.04	7.27	8.31	9.15	9.77	10.15

Figure 18: Ten-story base-isolated building.

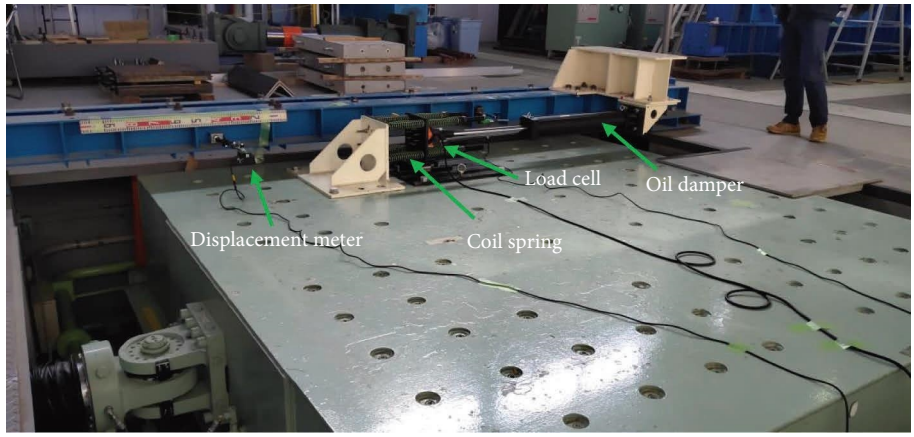

Figure 19: Real-time hybrid simulation (RTHS) of the analytical model.

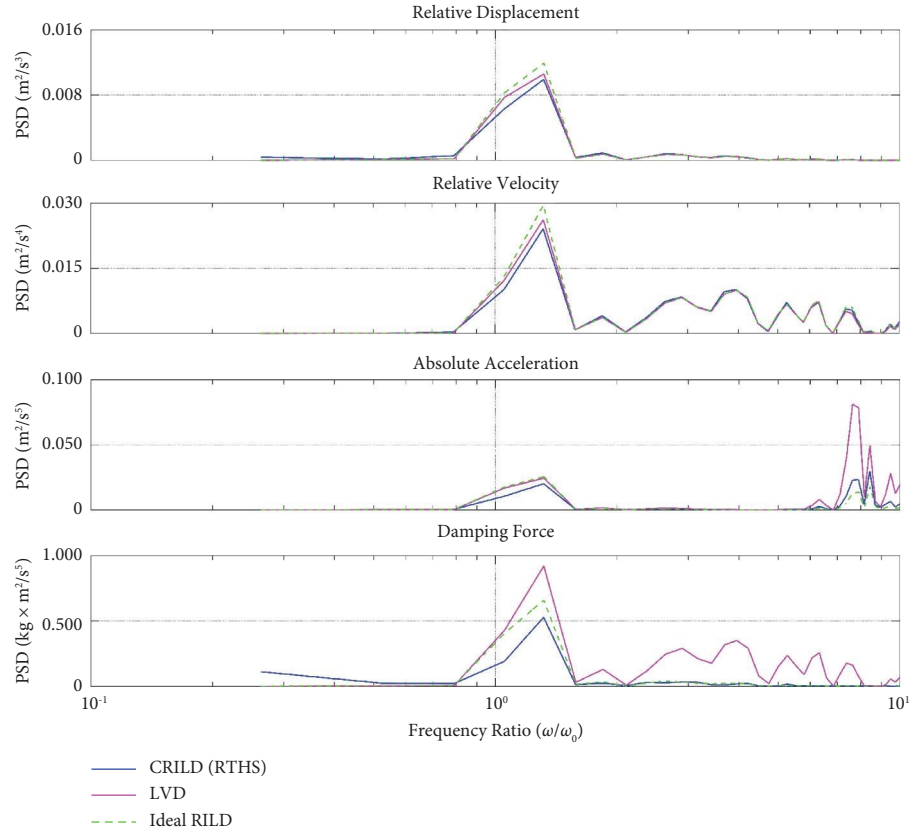

Figure 20: Power spectral densities (PSDs) of the isolation layer under the Kobe record.

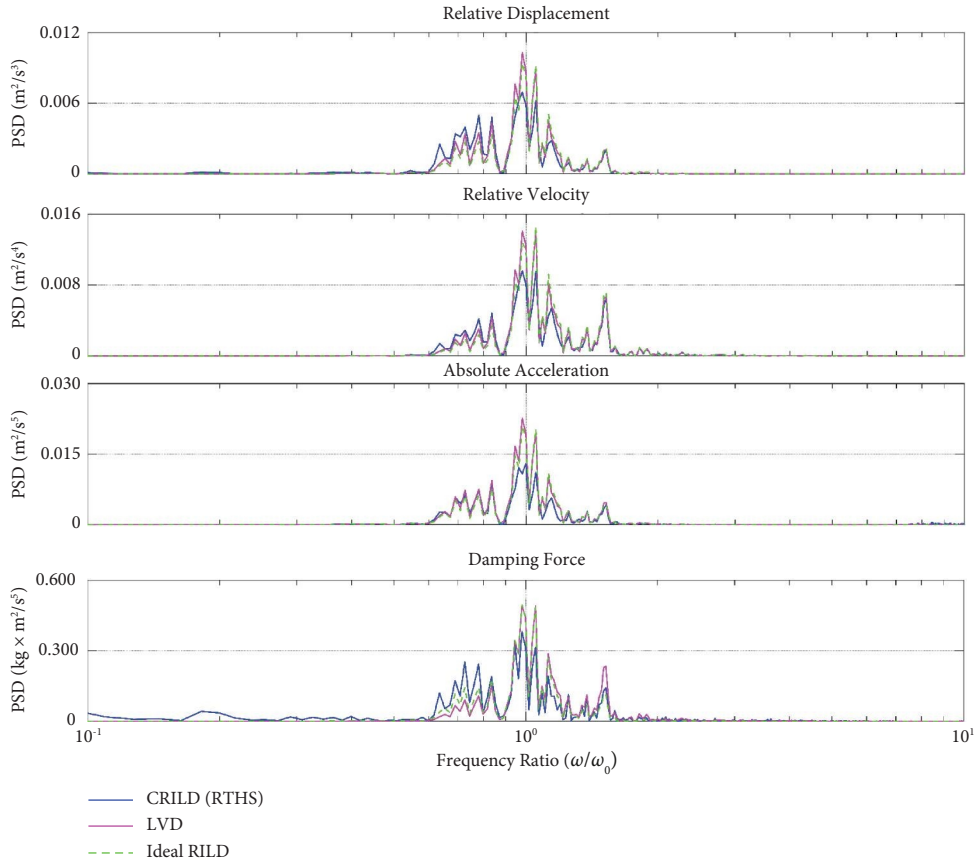

Figure 21: Power spectral densities (PSDs) of the isolation layer under the Tomakomai record.

5. Conclusions and Discussion

In this study, the impulse-response precursor and modal decomposition method were investigated for a nonproportionally distributed RILD system. RTHS experiments were also conducted to validate the proposed modal analysis method. The primary contributions and findings of this study are as follows:

(1) Owing to the noncausality of RILD, the expression for the preimpulse response was first derived to address the paucity of relevant studies concerning the nonproportionally distributed RILD system. Then, a modal decomposition method was developed for nonproportionally distributed RILD systems to offer an innovative method for performing modal analysis.

(2) To investigate the feasibility of the proposed methods for obtaining preimpulse and modal responses of the nonproportionally distributed RILD systems, a set of 2DOF systems and a ten-story structure were employed for numerical analysis. The proposed method provided a superior approximation of the peak dynamic responses of the RILD system as compared with the conventional FFT approach.

(3) The RILD and LVD systems had nearly equal modal displacements and velocities in the first mode. However, the displacement and velocity responses of the high modes of the system containing RILD were generally smaller than those containing LVD for the selected records. The RILD system was less accelerated in terms of modal acceleration. Maintaining a damping force lower than that of the LVD is an advantage of the RILD device.

(4) A coil spring and an oil damper were designed and manufactured to causally realize RILD. The RTHS experiments demonstrated the feasibility of realizing an ideal RILD using the CRILD device, which can provide a promising approach to mitigate the acceleration responses in the high modes of a high-rise building and maintain a lower damping force than in conventional LVD devices in the high-frequency region. In addition, the experimental results validated the effectiveness of the proposed modal analysis method.

This study is the first to investigate the impulse-response precursor and separated modal responses of multistory nonproportionally distributed RILD systems. It provides a novel approach for time-domain analysis of the noncausal RILD system. This study first reveals the differences in the modal responses between the RILD and LVD systems. However, the nonlinearity of the structures is ignored at the present stage owing to the associated complexity, and a structure containing hybrid types of damping is reserved for future studies. Furthermore, application of RILD-based devices in actual buildings remains to be studied.

Appendix

The modal coordinates can be expressed as follows [46]:

$$\begin{aligned} z_n^{R+}(t) &= S_n^{R+} e^{\lambda_n^+ t},\ \widehat{z}_n^{R+}(t) = \widehat{S}_n^{R+} e^{\widehat{\lambda_n^+} t}, \quad (\omega > 0), \\ z_n^{R-}(t) &= S_n^{R-} e^{\lambda_n^- t},\ \widehat{z}_n^{R-}(t) = \widehat{S}_n^{R-} e^{\widehat{\lambda_n^-} t}, \quad (\omega < 0). \end{aligned} \tag{A.1}$$

Therefore,

$$\begin{aligned} Z_n^{R+}(i\omega) = \mathscr{F}\left[z_n^{R+}(t)\right] &= \int_{-\infty}^{+\infty} \left(S_n^{R+} e^{\lambda_n^+ t}\right) e^{-i\omega t} dt = S_n^{R+} \int_0^{+\infty} e^{\left(\lambda_n^+ - i\omega\right)t} dt \\ &= S_n^{R+} \cdot \frac{e^{\left(\lambda_n^+ - i\omega\right)t}}{\lambda_n^+ - i\omega}\Bigg|_0^{+\infty} \overset{\because \mathrm{Real}\left(\lambda_n^+\right) < 0}{=} S_n^{R+}\left(0 - \frac{1}{\lambda_n^+ - i\omega}\right) = \frac{S_n^{R+}}{i\omega - \lambda_n^+}, \end{aligned} \tag{A.2}$$

where $\mathscr{F}[\cdot]$ is the symbol of the Fourier transform. Then, we obtain

$$\left(i\omega - \lambda_n^+\right) Z_n^{R+}(i\omega) - S_n^{R+} = 0. \tag{A.3}$$

For the case of $\omega < 0$, one needs to adopt the integral method proposed by Inaudi and Makris [36] and calculate the integration of the differential equations backwards in time for the modal coordinates associated with unstable poles. Therefore,

$$\begin{aligned} Z_n^{R-}(i\omega) &= \mathcal{F}\left[z_n^{R-}(t)\right] = \int_{+\infty}^{-\infty} \left(S_n^{R-} e^{\lambda_n^- t}\right) e^{-i\omega t} dt \overset{t' = -t}{=} \int_0^{+\infty} \left[S_n^{R-} e^{\lambda_n^-(-t')}\right] e^{-i\omega(-t')} d\left(-t'\right) \\ &= -S_n^{R-} \int_0^{+\infty} e^{\left(-\lambda_n^- + i\omega\right)t'} dt' = -S_n^{R-} \cdot \left. \frac{e^{\left(-\lambda_n^- + i\omega\right)t'}}{-\lambda_n^- + i\omega} \right|_{t'=0}^{t'=-\infty} \\ &\overset{\because \mathrm{Real}\left(\lambda_n^-\right) > 0}{=} -S_n^{R-} \left(0 - \frac{1}{-\lambda_n^- + i\omega}\right) = \frac{S_n^{R-}}{i\omega - \lambda_n^-}. \end{aligned} \tag{A.4}$$

Finally,

$$\left(i\omega - \lambda_n^-\right) Z_n^{R-}(i\omega) - S_n^{R-} = 0. \tag{A.5}$$

The Fourier transforms of the modal coordinates associated with unstable poles (this are $z_n^{R-}(t)$ and $\hat{z}_n^{R-}(t)$) are integrated backwards rather than forwards in time. Similarly, we obtain

$$\begin{aligned} \left(i\omega - \hat{\lambda}_n^+\right) \hat{Z}_n^{R+}(i\omega) - \hat{S}_n^{R+} &= 0, \\ \left(i\omega - \hat{\lambda}_n^-\right) \hat{Z}_n^{R-}(i\omega) - \hat{S}_n^{R-} &= 0. \end{aligned} \tag{A.6}$$

Data Availability

The data used to support the findings of this study are included within the article.

Conflicts of Interest

The authors declare that there are no conflicts of interest regarding the publication of this paper.

Authors' Contributions

Wei Liu was responsible for conceptualization, methodology writing the original draft, and funding acquisition. Yi-Qing Ni was responsible for supervision and funding acquisition.

Acknowledgments

This study was supported by the Postdoctoral Matching Scheme of Hong Kong Polytechnic University (1-W26C) and the China Scholarship Council (202008050036). The authors also acknowledge the funding support from the Innovation and Technology Commission (ITC) of the Hong Kong SAR Government to the Hong Kong Branch of the Chinese National Rail Transit Electrification and Automation Engineering Technology Research Center (Grant nos. K-BBY1 and ITS/096/21).

References

[1] W. Liu and K. Ikago, "Feasibility of physical implementation of rate-independent linear damping to protect multistory low-frequency structures," *Journal of Sound and Vibration*, vol. 528, Article ID 116893, 2022.

[2] S. H. Crandall, "Dynamic response of systems with structural damping," in *Air, Space, and Instruments, Draper Anniversary Volume*, S. Lees, Ed., pp. 183–193, McGraw-Hill Book Co, New York, NY, USA, 1963.

[3] S. H. Crandall, "The role of damping in vibration theory," *Journal of Sound and Vibration*, vol. 11, no. 1, p. 3, 1970.

[4] J. A. Inaudi and J. M. Kelly, "Linear hysteretic damping and the Hilbert transform," *Journal of Engineering Mechanics*, vol. 121, no. 5, pp. 626–632, 1995.

[5] N. O. Myklestad, "The concept of complex damping," *Journal of Applied Mechanics*, vol. 19, no. 3, pp. 284–286, 1952.

[6] R. Bishop, "The treatment of damping forces in vibration theory," *The Journal of the Royal Aeronautical Society*, vol. 59, no. 539, pp. 738–742, 1955.

[7] M. A. Biot, "Linear thermodynamics and the mechanics of solids," in *Proceedings of the 3rd U.S. National Congress on Applied Mechanics*, New York, NY, USA, June 1958.

[8] T. K. Caughey, "Vibration of dynamic systems with linear hysteretic damping (linear theory)," in *Proceedings of the 4th U.S. National Congress on Applied Mechanics*, New York, NY, USA, August 1962.

[9] N. Makris and M. Constantinou, "Fractional-derivative Maxwell model for viscous dampers," *Journal of Structural Engineering*, vol. 117, no. 9, pp. 2708–2724, 1991.

[10] G. B. Muravskii, "On frequency independent damping," *Journal of Sound and Vibration*, vol. 274, no. 3-5, pp. 653–668, 2004.

[11] N. Nakamura, "Practical causal hysteretic damping," *Earthquake Engineering and Structural Dynamics*, vol. 36, no. 5, pp. 597–617, 2007.

[12] P. D. Spanos and S. Tsavachidis, "Deterministic and stochastic analyses of a nonlinear system with a Biot visco-elastic element," *Earthquake Engineering and Structural Dynamics*, vol. 30, no. 4, pp. 595–612, 2001.

[13] N. Makris, "Causal hysteretic element," *Journal of Engineering Mechanics*, vol. 123, pp. 1209–1214, 1997.

[14] P. D. Spanos and G. I. Evangelatos, "Response of a non-linear system with restoring forces governed by fractional derivatives–time domain simulation and statistical linearization solution," *Soil Dynamics and Earthquake Engineering*, vol. 30, no. 9, pp. 811–821, 2010.

[15] K. J. Parker, "Real and causal hysteresis elements," *Journal of the Acoustical Society of America*, vol. 135, no. 6, pp. 3381–3389, 2014.

[16] G. B. Muravskii, "Linear models with nearly frequency independent complex stiffness leading to causal behaviour in time domain," *Earthquake Engineering and Structural Dynamics*, vol. 36, no. 1, pp. 13–33, 2007.

[17] Y. Huang, R. Sturt, and M. Willford, "A damping model for nonlinear dynamic analysis providing uniform damping over a frequency range," *Computers and Structures*, vol. 212, pp. 101–109, 2019.

[18] G. Genta and N. Amanti, "On the equivalent viscous damping for systems with hysteresis," *Solid Mechanics*, vol. 32, pp. 21–43, 2009.

[19] A. Reggio and M. De Angelis, "Modelling and identification of structures with rate-independent linear damping," *Mechanics*, vol. 50, no. 3, pp. 617–632, 2015.

[20] P. Deastra, D. Wagg, N. Sims, and M. Akbar, "Tuned inerter dampers with linear hysteretic damping," *Earthquake Engineering and Structural Dynamics*, vol. 49, no. 12, pp. 1216–1235, 2020.

[21] A. A. Sarlis, D. T. R. Pasala, M. Constantinou, A. Reinhorn, S. Nagarajaiah, and D. Taylor, "Negative stiffness device for seismic protection of structures," *Journal of Structural Engineering*, vol. 139, no. 7, pp. 1124–1133, 2013.

[22] A. Sarlis, D. Pasala, M. C. Constantinou, A. M. Reinhorn, S. Nagarajaiah, and D. P. Taylor, "Negative stiffness device for seismic protection of structures: shake table testing of a seismically isolated structure," *Journal of Structural Engineering*, vol. 142, Article ID 04016005, 2016.

[23] S. Nagarajaiah, L. Chen, and M. Wang, "Adaptive stiffness structures with dampers: seismic and wind response reduction using passive negative stiffness and inerter systems," *Journal of Structural Engineering*, vol. 148, no. 11, Article ID 04022179, 2022.

[24] H. Luo, K. Ikago, C. Chong, A. Keivan, and B. M. Phillips, "Performance of low-frequency structures incorporated with rate-independent linear damping," *Engineering Structures*, vol. 181, pp. 324–335, 2019.

[25] A. Keivan, B. M. Phillips, M. Ikenaga, and K. Ikago, "Causal realization of rate-independent linear damping for the protection of low-frequency structures," *Journal of Engineering Mechanics*, vol. 143, no. 9, Article ID 04017058, 2017.

[26] A. Keivan, B. M. Phillips, and K. Ikago, "Adaptive causal realization of rate-independent linear damping," *Engineering Structures*, vol. 167, pp. 256–271, 2018.

[27] A. Keivan, R. Y. Zhang, D. Keivan, B. M. Phillips, M. Ikenaga, and K. Ikago, "Rate-independent linear damping for the improved seismic performance of inter-story isolated structures," *Journal of Earthquake Engineering*, vol. 26, no. 2, pp. 793–816, 2020.

[28] W. Liu and K. Ikago, "Causal implementation of rate-independent linear damping for the seismic protection of low-frequency structures," *Structures*, vol. 35, pp. 274–288, 2022.

[29] W. Liu, K. Ikago, Z. Wu, and I. Fukuda, "Modified tuned Maxwell–Wiechert model for improving seismic performance of base-isolated structures," *Journal of Building Engineering*, vol. 54, Article ID 104616, 2022.

[30] W. Liu and K. Ikago, "Feasibility study of the physical implementation of rate-independent linear damping for the protection of low-frequency structures," *Journal of Building Engineering*, vol. 44, Article ID 103319, 2021.

[31] W. Liu and K. Ikago, "Feasibility study of a passive rate-independent damping device for the seismic protection of low-frequency structures," *Structures*, vol. 34, pp. 2499–2514, 2021.

[32] W. Liu and K. Ikago, "Performance of a passive rate-independent damping device in a seismically isolated multistory building," *Structural Control and Health Monitoring*, vol. 29, no. 6, 2022.

[33] W. Liu and K. Ikago, "Experimental study of earthquake input energy of low-frequency structures equipped with a passive rate-independent damping device," *Structural Control and Health Monitoring*, vol. 29, no. 2, 2022.

[34] W. Liu and J. Liu, "Experimental realization of rate-independent linear damping using a semiactive damper to enhance the seismic performance of low-frequency structures," *Journal of Building Engineering*, vol. 70, Article ID 106374, 2023.

[35] W. Liu, Y. Q. Ni, K. Ikago, and W. K. Ao, "Seismic control of base-isolated structures using rate-independent damping devices," *Journal of Building Engineering*, vol. 78, Article ID 107744, 2023.

[36] J. A. Inaudi and N. Makris, "Time domain analysis of linear hysteretic damping," *Earthquake Engineering and Structural Dynamics*, vol. 25, no. 6, pp. 529–545, 1996.

[37] H. C. Tsai and T. C. Lee, "Dynamic analysis of linear and bilinear oscillators with rate-independent damping," *Computers and Structures*, vol. 80, no. 2, pp. 155–164, 2002.

[38] K. F. Chen and S. W. Zhang, "On the impulse-response precursor of an ideal linear hysteretic damper," *Journal of Sound and Vibration*, vol. 312, no. 4-5, pp. 576–583, 2008.

[39] K. F. Chen and Y. H. Shen, "The impulse-response of a band-limited vibrator with rate-independent hysteretic damping," *Mechanical Journal*, vol. 199, no. 1-4, pp. 17–28, 2008.

[40] G. B. Warburton and S. R. Soni, "Errors in response calculations for non-classically damped structures," *Earthquake Engineering and Structural Dynamics*, vol. 5, no. 4, pp. 365–376, 1977.

[41] M. Simon and G. R. Tomlinson, "Use of the Hilbert transform in modal analysis of linear and non-linear structures," *Journal of Sound and Vibration*, vol. 96, no. 4, pp. 421–436, 1984.

[42] A. K. Chopra, "Modal analysis of linear dynamic systems: physical interpretation," *Journal of Structural Engineering*, vol. 122, no. 5, pp. 517–527, 1996.

[43] D. J. Ewins, *Modal Testing: Theory, Practice and Application*, Research Studies Press LTD, Boston, MA, USA, 2000.

[44] M. William, H. Richard, and D. Z. Ronald, *Matrix Structural Analysis*, Wiley, Hoboken, NJ, USA, 1999.

[45] A. S. Veletsos and C. E. Ventura, "Modal analysis of non-classically damped linear systems," *Earthquake Engineering and Structural Dynamics*, vol. 14, no. 2, pp. 217–243, 1986.

[46] A. K. Chopra, "Dynamics of structures: theory and applications to earthquake engineering," in *SI Units*, Pearson Education Limited, London, UK, 5th edition, 2020.

[47] T. Igusa and A. Der Kiureghian, "Dynamic characterization of two-degree-of-freedom equipment-structure systems," *Journal of Engineering Mechanics*, vol. 111, no. 1, pp. 1–19, 1985.

[48] J. N. Yang, S. Sarkani, and F. X. Long, "A response spectrum approach for analysis of nonclassically damped structures," Technical report NCEER-88-0020, University at Buffalo, Buffalo, NY, USA, 1988.

[49] R. Sinha and T. Igusa, "CQC and SRSS methods for non-classically damped structures," *Earthquake Engineering and Structural Dynamics*, vol. 24, no. 4, pp. 615–619, 1995.

[50] A. K. Gupta, T. Hassan, and A. Gupta, "Correlation coefficients for modal response combination of non-classically damped systems," *Nuclear Engineering and Design*, vol. 165, no. 1-2, pp. 67–80, 1996.

[51] G. Oliveto, A. Santini, and E. Tripodi, "Complex modal analysis of a flexural vibrating beam with viscous end conditions," *Journal of Sound and Vibration*, vol. 200, no. 3, pp. 327–345, 1997.

[52] S. Di Lorenzo, M. Di Paola, G. Failla, and A. Pirrotta, "On the moving load problem in Euler–Bernoulli uniform beams with viscoelastic supports and joints," *Mechanical Journal*, vol. 228, no. 3, pp. 805–821, 2017.

[53] B. Hirzinger, C. Adam, and P. Salcher, "Dynamic response of a non-classically damped beam with general boundary conditions subjected to a moving mass-spring-damper system," *International Journal of Mechanical Sciences*, vol. 185, Article ID 105877, 2020.

[54] H. T. Chen, Y. H. Liu, and P. Tan, "Generalized complex mode superposition approach for non-classically damped systems," *Structural Engineering and Mechanics*, vol. 73, pp. 271–286, 2020.

[55] G. Qiao and S. Rahmatalla, "Dynamics of Euler-Bernoulli beams with unknown viscoelastic boundary conditions under a moving load," *Journal of Sound and Vibration*, vol. 491, Article ID 115771, 2021.

[56] H. T. Chen, P. Tan, and F. L. Zhou, "An improved response spectrum method for non-classically damped systems," *Bulletin of Earthquake Engineering*, vol. 15, no. 10, pp. 4375–4397, 2017.

[57] S. H. Crandall, "Dynamic response of systems with structural damping," *Air Force Office of Scientific Research*, pp. 1–19, 1961.

[58] K. A. Foss, "Coordinates which uncouples the equations of motion of damped linear dynamic systems," *Journal of Applied Mechanics*, vol. 32, pp. 361–364, 1958.

[59] Architectural Institute of Japan, *Design Recommendations for Seismically Isolated Buildings*, Architectural Institute of Japan, Tokyo, Japan, 4th edition, 2016.

[60] NIED, "National research institute for earth science and disaster resilience," 2023, http://www.bosai.go.jp.

[61] S. Midorikawa and H. Miura, "Re-digitization of strong motion accelerogram at Hachinohe harbor during the 1968 Tokachi-Oki, Japan Earthquake," *Journal of Japan Association for Earthquake Engineering*, vol. 10, no. 2, pp. 12–21, 2010.

[62] K. Ikago, Y. Sugimura, K. Saito, and N. Inoue, "Modal response characteristics of a multiple-degree-of freedom structure incorporated with tuned viscous mass dampers," *Journal of Asian Architecture and Building Engineering*, vol. 11, no. 2, pp. 375–382, 2012.

[63] K. Takanashi and M. Nakashima, "Japanese activities on online testing," *Journal of Engineering Mechanics*, vol. 113, pp. 1014–1032, 1987.

[64] P. B. Shing, M. Nakashima, and O. S. Bursi, "Application of pseudodynamic test method to structural research," *Earthquake Spectra*, vol. 12, no. 1, pp. 29–56, 1996.